We are IntechOpen,
the world's leading publisher of
Open Access books
Built by scientists, for scientists

4,800
Open access books available

122,000
International authors and editors

135M
Downloads

Our authors are among the

154
Countries delivered to

TOP 1%
most cited scientists

12.2%
Contributors from top 500 universities

CLARIVATE ANALYTICS
BOOK
CITATION
INDEX
INDEXED

WEB OF SCIENCE™

Selection of our books indexed in the Book Citation Index
in Web of Science™ Core Collection (BKCI)

Interested in publishing with us?
Contact book.department@intechopen.com

Numbers displayed above are based on latest data collected.
For more information visit www.intechopen.com

Thermoelectric and Topological Insulator Bismuth Chalcogenide Thin Films Grown Using Pulsed Laser Deposition

Phuoc Huu Le and Chih Wei Luo

Additional information is available at the end of the chapter

Abstract

Bismuth chalcogenides have been intensively studied for their high-performance thermoelectric properties and their novel topological surface states, which could significantly benefit novel applications in fields such as TE devices, spintronics, and quantum computing. This chapter reports recent advances in pulsed laser deposition (PLD) for the growth of bismuth chalcogenide (e.g., Bi_2Te_3, Bi_2Se_3, and Bi_3Se_2Te) thin films and their novel properties. It covers a wide range of fields such as thin film growth using PLD for fabricating polycrystalline and epitaxial films with different thermoelectric, nanomechanical, and magnetotransport properties as a function of the PLD processing conditions. Moreover, the proximity-induced superconductivities in Bi inclusions/ bismuth chalcogenide thin films are also reported and discussed in detail.

Keywords: pulsed laser deposition, thermoelectrics, topological insulators, bismuth chalcogenides, superconductivity, magnetoresistance

1. Introduction

Bismuth chalcogenide thin films are of great interest because of the exciting properties of topological insulators (TIs) and their applications to thermoelectrics (TEs). These materials have been applied in integrated TE cooling devices working at near room temperature [1, 2]. TIs are exotic materials with an insulating bulk and topologically protected states on the surface which could be used in different applications, such as spintronics and quantum computing [3–6]. The topological surface states (TSSs) exhibit Dirac linear energy dispersion

inside the bulk gap, spin-polarization by spin-momentum locking nature, and weak anti-localization (WAL) due to the strong spin-orbit coupling [3–6]. Thus, the WAL through magnetotransport studies has been widely used as a signature of TI materials [7–9].

For application purposes, thin film growth techniques for TE and TI materials are required. Among physical vapor deposition techniques, pulsed laser deposition (PLD) offers great versatility in growing polycrystalline and epitaxial thin films with high growth rates, multiple elements, and diverse structural morphologies for both fundamental studies and applications. The purpose of this chapter is to outline recent advances in the PLD growths of bismuth chalcogenide thin films with desired properties for TE/TI applications and fundamental studies.

2. Thin film growth using pulsed laser deposition (PLD)

Thin film growth consists of nucleation, growth, and coalescence (**Figure 1a**). In a physical vapor deposition, an extremely nonequilibrium process takes place at high supersaturations and at comparatively high concentrations of impure atoms [10]. Nucleation takes place at high supersaturations S (defined as $S = p/p_e$, where p is the vapor pressure of the deposited material evaporated from the source at temperature T and p_e is the equilibrium vapor pressure of the substrate material at temperature T_S). The incident vapor arrives at the surface of substrates and then forms small but highly mobile clusters or islands with uniform distribution. In this stage, the impinging atoms and subcritical clusters are incorporated and consequently increase their sizes, while the island density rapidly saturates. In the following stage, the islands are emerged via a coalescence phenomenon which is liquid-like for some cases, especially at high substrate temperatures. Coalescence leads to a decrease in island density and forms local denuding positions on the surface of substrates where further nucleation can then occur (**Figure 1a**) [11]. The sequence of film nucleation and growth events can be well appreciated in the transmission electron microscopy (TEM) images in **Figure 1b–d** [11].

2.1. Basic growth modes

For all phase transitions, the formation of thin films is characterized by the formation of nuclei and their growth. Depending on the interaction energies of substrate atoms and film atoms, any of three growth modes in **Figure 2a–c** can occur:

- 2D Frank-van der Merwe mode: layer-by-layer growth, in which the interaction between substrate and atoms of film is greater than that between adjacent atoms of film.

- 3D Volmer-Weber mode: separated islands form on the surface of substrates, in which the interaction between atoms of film is greater than that between a substrate and the adjacent atoms of film.

- Stranski-Krastanov mode: layer plus island, in which one or two monolayers form first and then grow individually.
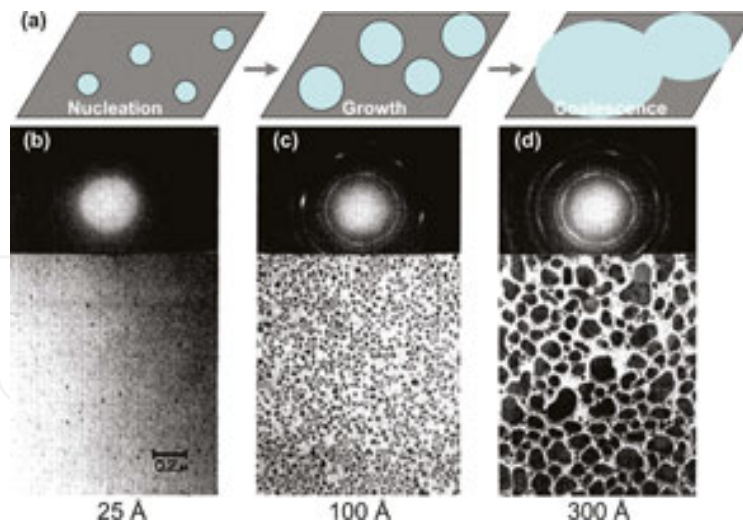
Figure 1. (a) Schematics of thin film growth processes: nucleation, growth, coalescence. Transmission electron microscope images of (b) nucleation, (c) growth, and (d) coalescence of Ag films on (1 1 1) NaCl substrates. Corresponding diffraction patterns are shown.
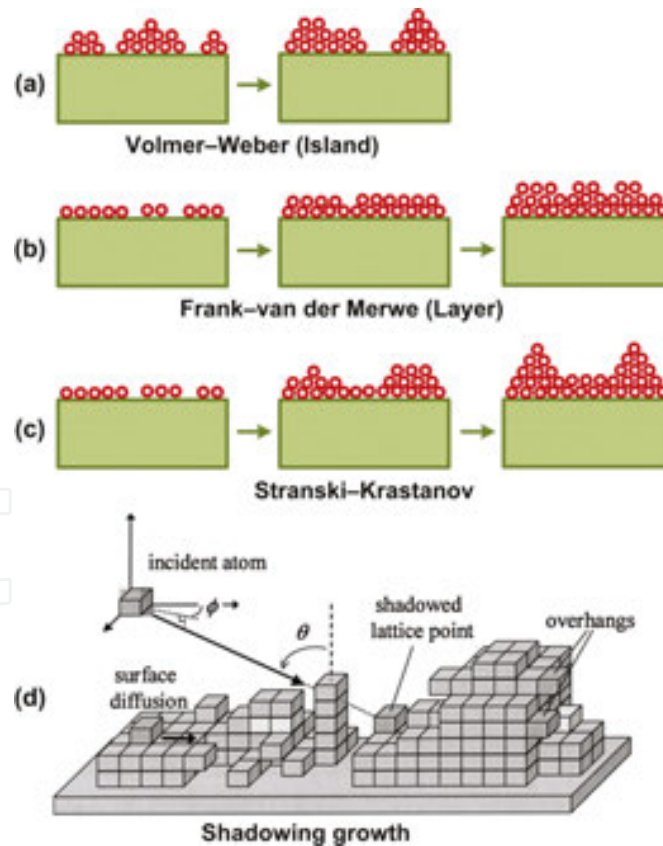

Figure 2. Basic modes of thin film growth: (a) island in the Volmer-Weber mode, (b) layer by layer in the two-dimensional Frank-van der Merwe mode, (c) layer plus island in the Stranski-Krastanov mode. (d) Shadowing growth: a schematic of three-dimensional Monte Carlo simulations for oblique angle deposition [13].

After an initially random nucleation of islands on the surface of the substrates, the deposition on the top of the islands is faster than that in the valleys due to the oblique incident flux (the so-called **shadowing effect**) [12, 13]. Isolated columns are therefore formed on these islands during subsequent growths (**Figure 2d**) [13].

2.2. Epitaxy growth

Epitaxy refers to the growth of a single crystal film on top of a single crystal substrate. The deposited film is denoted as an epitaxial film or epitaxial layer. The growth is called homoepitaxy if the film and the substrate are the same material, and it is called heteroepitaxy if they are different materials. Epitaxial relationship is determined as: $(HKL) \parallel (hkl)$; $[UVW] \parallel [uvw]$, where (hkl) and (HKL) are the Miller indices of the overgrowth plane and substrate at the common interface. The corresponding parallel directions in the overgrowth and substrate planes, denoted by $[wuw]$ and $[UVW]$, respectively, must also be specified.

2.3. Factors governing the epitaxy growth

The key factors governing epitaxy growths are structural compatibility, chemical compatibility, and growth temperatures.

- **Structural compatibility:** The structures of a film and a substrate should have good lattice matching in terms of crystal structures ($a_{0,\,sub}$) and lattice constants ($a_{0,\,film}$), that is, small lattice misfit.

Lattice misfit f:

$$f = \frac{a_{0,sub} - a_{0,film}}{a_{0,film}} \approx \frac{a_{0,sub} - a_{0,film}}{a_{0,sub}} \sqrt{2}. \tag{1}$$

- **Chemical compatibility:** This includes chemical bonding and chemical diffusion.

- **Growth temperatures:** Good epitaxy growth is obtained at above or around the well-defined elevated substrate temperature (T_e). T_e depends on the deposition rate, particle energy, and surface contamination. Generally, a higher temperature is recommended to reduce surface contamination by desorption (or enhance surface mobility) of atoms to reach the favorable sites and also enhance the diffusivity in deposition for favoring re-crystallization and defect annihilation.

2.4. Preparation of bismuth chalcogenide films by PLD

PLD is one of the most convenient thin film growth techniques that uses a high-intensity pulsed laser beam as an external energy source to ablate a target, form a plume, and then deposit thin films onto a substrate. **Figure 3** shows a typical PLD system for preparing TE and TI thin films. A substrate is heated and maintained at a desired substrate temperature (T_S) using a thermocouple and a proportional-integral-derivative temperature controller. The thermocouple was

buried inside a stainless steel substrate holder, which is heated by a tungsten lamp just behind the holder. The pressure of ambient gas (He/Ar) can be fine-tuned by the needle valve. A KrF excimer laser beam (λ = 248 nm, pulsed duration of 15–20 ns, repetition rate in the range of 1–15 Hz, and fluence of 1–10 J/cm^2) is guided by several UV mirrors and focused on a stoichiometric polycrystalline or a single crystal target (e.g., Bi_2Te_3, Bi_2Se_3, Bi_2Se_2Te) within the vacuum chamber by a UV lens. The target-to-substrate distance was 40 mm. During the deposition of Bi_2Se_3 films, pure (6N) He/Ar gas was introduced into the vacuum chamber, which was evacuated to a base pressure of 4×10^{-4} Pa (or 3×10^{-6} Torr) and maintained at a certain constant pressure (P), using a differential evacuation system.
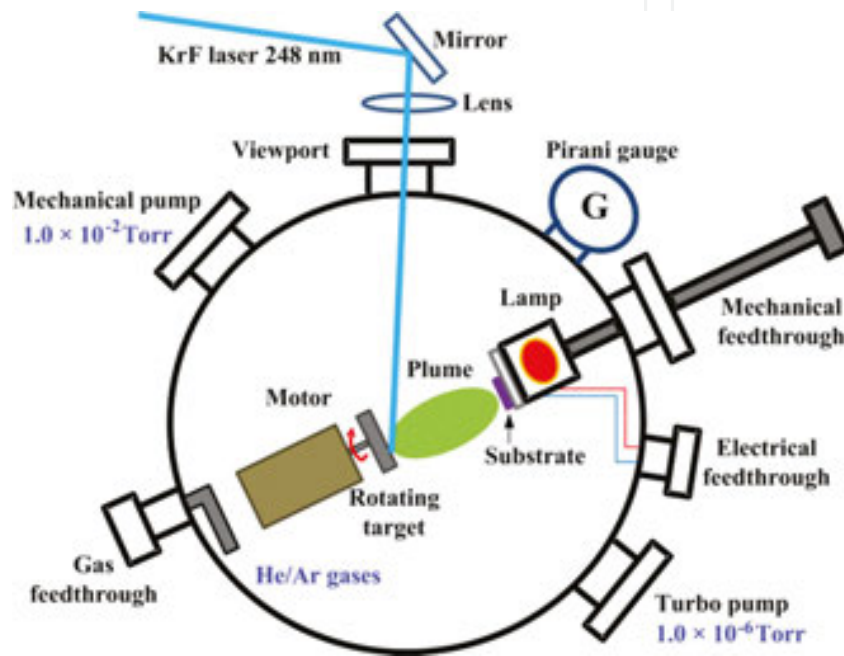

Figure 3. Schematic illustration of a pulsed laser deposition (PLD) system. G: gauge.

The surface of substrates should be atomically clean and free from impurities because the contaminants can interact with the thin films being deposited and substantially degrade its quality and adhesion to the substrates. The presence of unwanted surface contaminants can also influence the growth and orientation of the films in an undesired manner. In the depositions for TE thin films, an approximately 300-nm-thick SiO_2 layer was thermally grown on the Si wafers (thickness 525 μm) for electrical isolation purpose. The wafers were cut into 1.5 cm × 1.5 cm substrates. The substrates were cleaned with acetone to dissolve any contaminants adhering to the surface of substrates such as grease and oils. This was followed by rinsing with methanol to remove any residues left behind after cleaning with acetone. Afterward, the substrates were rinsed in distilled water and dried with nitrogen flow. The substrates were then used for the deposition of TE thin films.

Here are some examples of PLD growth of TE films. For Bi_2Se_3 thin films, the depositions were at T_S of 200–350°C and helium ambient pressure (P) of 0.7–173 Pa. The number of laser pulses was 9000 and the deposition took 30 min. The average growth rate was approximately 0.46 Å/

pulse [14]. For the growth of Bi_2Te_3 thin films, T_S was varied from room temperature (30°C) to 380°C and the Ar ambient pressure (P_{Ar}) was at 80 Pa. The number of laser pulses was 12,000 and the deposition took 40 min. The average growth rate was approximately 0.52 Å/pulse [15]. For the growth of Bi-Se-Te thin films, the depositions were at T_S of 200–350°C and a helium ambient pressure (P_{He}) of 0.027–86.7 Pa. The number of laser pulses was 9000 and the deposition took 15 min. The average growth rate was approximately 0.6 Å/pulse [16].

3. Thermoelectric bismuth chalcogenide thin films

3.1. Crystal structures of bismuth chalcogenides

The crystal structures of bismuth chalcogenides (e.g., Bi_2Te_3, Bi_2Se_3, and Bi_3Se_2Te) are usually described by a hexagonal cell consisting of 15 layers of atoms stacking along the *c*-axis with a sequence shown below [17], as shown in **Figure 4a** and **b**.
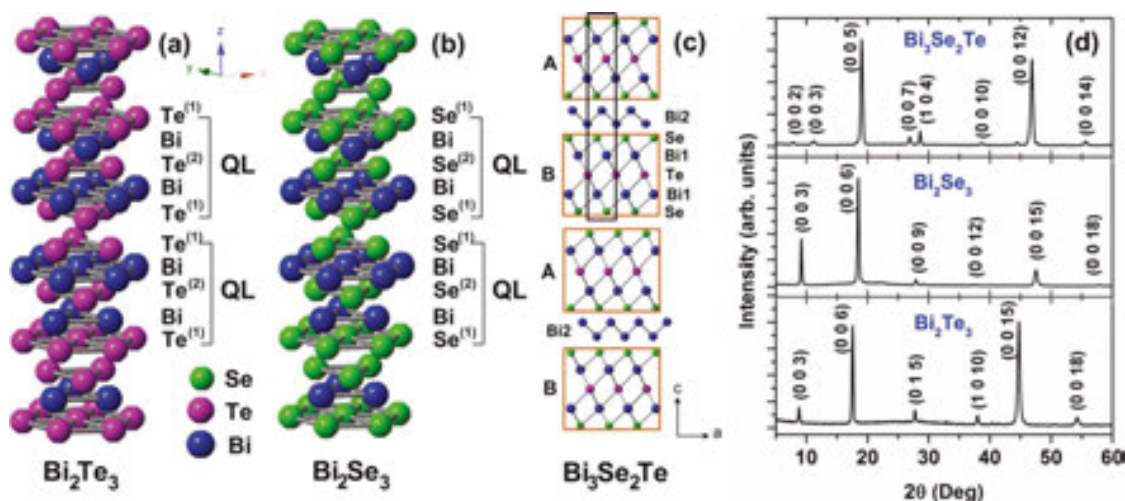

Figure 4. Crystal structures of (a) Bi_2Te_3, (b) Bi_2Se_3, and (c) Bi_3Se_2Te in the form of $(Bi_2)_m(Bi_2Se_2Te)_n$ (*m* = 1, *n* = 2) homologous series. The unit cells are marked with black thick boxes. (d) X-ray diffraction patterns of the typical TE bismuth chalcogenide thin films grown at 300°C on SiO_2/Si substrates.

A 5-atomic-layer-thick lamellae of -$(Te^{(1)}$-Bi-$Te^{(2)}$-Bi-$Te^{(1)})$- or -$(Se^{(1)}$-Bi-$Se^{(2)}$-Bi-$Se^{(1)})$- is called a quintuple layer, QL, in which the $Te^{(1)}$-Bi and Bi-$Te^{(2)}$ or $Se^{(1)}$-Bi and Bi-$Se^{(2)}$ are ionic-covalent bonds. Because of the weak binding (i.e., Van der Waals force) between Te or Se layers, bismuth chalcogenides could be cleaved easily along the plane perpendicular to the *c*-axis. It also induces the anisotropic thermal/electrical transport properties. For example, the thermal conductivity along the plane perpendicular to the *c*-axis (~1.5 W m^{-1} K^{-1}) is nearly two times higher than that along the *c*-axis direction (~0.7 W m^{-1} K^{-1}) [17, 18].

The crystal structures of Bi_3Se_2Te can be formed by ordered stacking of Bi_2Se_2Te and Bi_2 building blocks, that is, $(Bi_2)_m(Bi_2Se_2Te)_n$ (*m* = 1, *n* = 2) [19, 20], in which the covalently connected double layers of bismuth (Bi–Bi) lie between two QL (Se-Bi-Te-Bi-Se) blocks (**Figure 4c**); the (Bi–Bi)

strictly alternates with two QL (Se–Bi–Te–Bi–Se) blocks [9, 20]. **Figure 4d** shows the typical XRD patterns of Bi_2Te_3, Bi_2Se_3, and Bi_3Se_2Te thin films grown on SiO_2/Si substrates at $T_S = 300°C$. They exhibit the dominance of (0 0 1) family planes of the rhombohedral phases of Bi_2Te_3 (PDF#82-0358), Bi_2Se_3 (PDF#33-0214), and Bi_3Se_2Te (JCPDS 00-053-1190), indicating that the films are highly c-axis oriented (i.e., textured films).

3.2. Introduction to thermoelectrics and applications

Thermoelectric materials are solid-state energy converters in which the combination of thermal, electrical, and semiconducting properties allows them to be used to convert waste heat into electricity or electrical power directly into cooling and heating [21].

3.2.1. The thermoelectric figure of merit (ZT)

The performance of the thermoelectric materials is often denoted as figure of merit Z whose unit is K^{-1} or ZT with the dimensionless unit [17, 22].

$$ZT = \frac{\alpha^2 \sigma}{\kappa} T = \frac{\alpha^2 \sigma}{\kappa_E + \kappa_L} T \tag{2}$$

where σ, α, κ, and T are the electrical conductivity, Seebeck coefficient, thermal conductivity, and absolute temperature, respectively. The total thermal conductivity can be split into a lattice contribution (κ_L) and an electronic contribution (κ_E). The quantity $\alpha^2 \sigma$ is commonly used to represent the thermoelectric power factor (PF).

The efficiency of a thermoelectric device is directly related to ZT. For power generation, the maximum efficiency (η) is expressed by [23]

$$\eta = \frac{T_h - T_c}{T_h} \cdot \frac{\sqrt{1 + Z\bar{T}} - 1}{\sqrt{1 + Z\bar{T}} + \frac{T_c}{T_h}} \tag{3}$$

and for air-conditioning or refrigeration, the coefficient of performance is [23]

$$COP = \frac{T_c}{T_h - T_c} \cdot \frac{\sqrt{1 + Z\bar{T}} - \frac{T_h}{T_c}}{\sqrt{1 + Z\bar{T}} + 1} \tag{4}$$

where T_h and T_c are the hot-end and cold-end temperatures of the thermoelectric materials, respectively, and $\bar{T}$ is the average temperature of T_h and T_c. Therefore, the enhanced ZT value of TE materials is important to increase the COP for practical applications.

3.2.2. Conflicting properties in thermoelectric materials

Maximizing ZT is challenging due to the interdependence of the TE parameters. An increased power factor $\alpha^2\sigma$ by optimizing the carrier concentration n and/or a reduced lattice thermal conductivity κ_L by introducing the scattering centers are necessary to enhance ZT value. The dependences of these parameters with scattering factor r, carrier effective mass m^*, carrier mobility μ, and their interconnectivity limits the ZT to about 1 in large bulk materials [24].

The electrical conductivity (σ) and electrical resistivity (ρ) are related to n through the carrier mobility μ:

$$1/\rho = \sigma = ne\mu \tag{5}$$

The Wiedemann-Franz Law [2] states that the electronic contribution to the thermal conductivity is proportional to the electrical conductivity (σ) of the materials, with the relationship being

$$\kappa_e = L\sigma T = ne\mu LT \tag{6}$$

where e is electron charge, and L is the Lorenz factor of 2.48×10^{-8} J^2/K^2 C^2 for free electrons and this can vary particularly with carrier concentration [2].

The kinetic definition of α is the energy difference between the average energy of mobile carriers and the Fermi energy [25]. An increase in n leads to the increase in both the Fermi energy and the average energy, but the former increases more rapidly than the latter and thus results in a decrease in α value and a reduction factor of α^2n. Thus, in attempting to increase ZT for most of the homogeneous materials, the carrier concentration (n) increases electrical conductivity (σ) but reduces the Seebeck coefficient (α). For this reason, in metals and degenerate semiconductors (energy-independent scattering approximation), the Seebeck coefficient can be expressed as [2]:

$$\alpha = \frac{8\pi^2 k_B^2}{3eh^2} m^* T \left(\frac{\pi}{3n}\right)^{2/3} \tag{7}$$

The high m^* causes the Seebeck coefficient to rise according to Eq. (7). High m^* materials generally possess low μ which limits the enhancement of power factor by $(m^*)^{3/2}\mu$. Noticeably, the defect scatters are not only the phonons but also the electrons which lead to reduce κ_L as well as μ. Therefore, the ratio of μ/κ_L determines the improvement in ZT [17, 24]. Although the increase in the ratio is usually experimentally achieved through a greater reduction in κ_L rather than that in μ, some fundamental issues in this mechanism are not understood well [24].

Figure 5 shows the compromise between large α and high σ in thermoelectric materials that must be struck to maximize the figure of merit ZT. Meanwhile, the low carrier concentration

will result in lower electrical conductivity with decreasing ZT. The ZT and PF peaks typically occur at carrier concentrations between 10^{19} and 10^{21} carriers per cm^3 (depending on the material system), which fall in between common metals and semiconductors, that is, the concentrations found in heavily doped semiconductors [2].
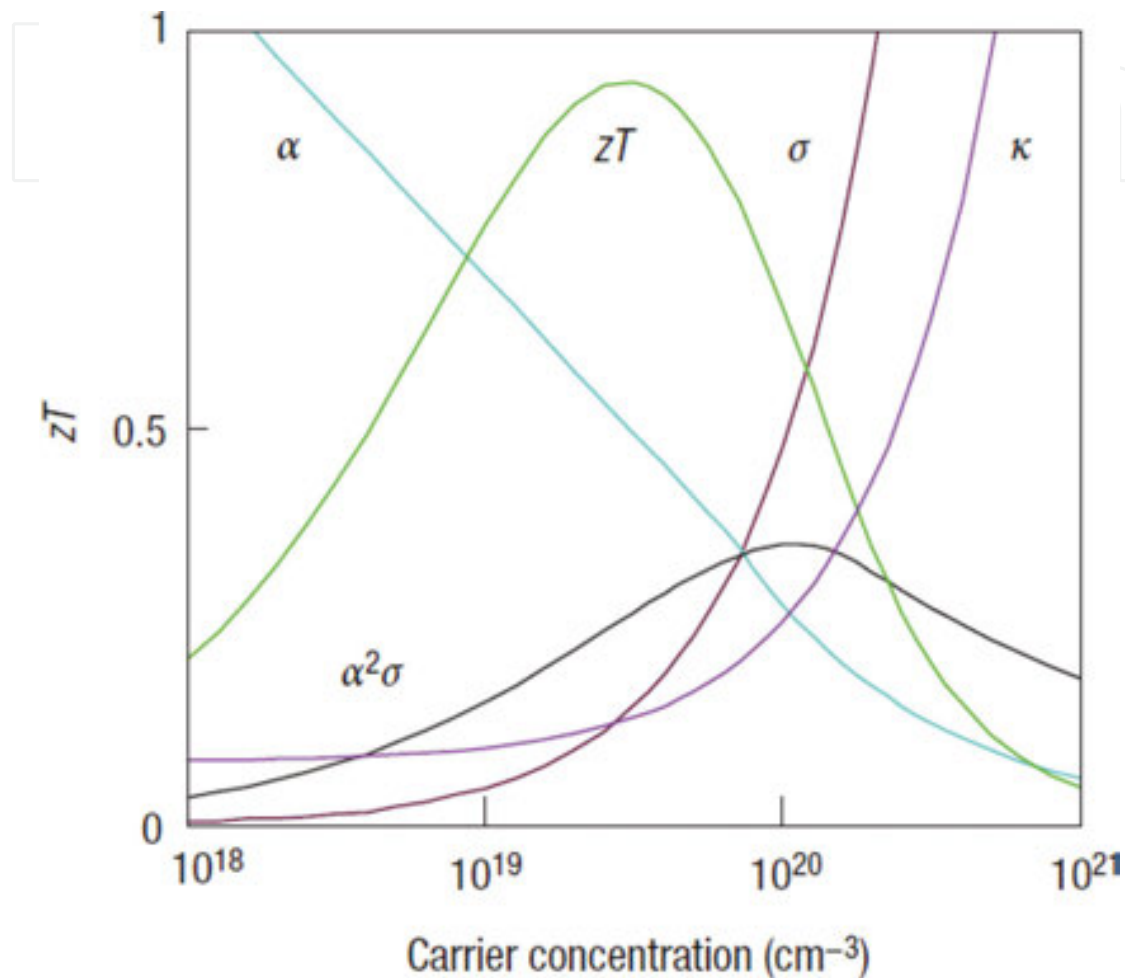

Figure 5. Maximizing the efficiency (ZT) of a thermoelectric device involves a compromise of thermal conductivity (κ, plotted on the y-axis from 0 to a top value of 10 W m^{-1} K^{-1}) and Seebeck coefficient (α, 0–500 μV K^{-1}) with electrical conductivity (σ, 0–5000 Ω^{-1} cm^{-1}) [2].

3.2.3. Overview of thermoelectric applications

TE devices have unique features: no moving parts, substantially less maintenance, quiet operation, high power density, low environmental impact, and high reliability [26]. Commercial use has been made mostly from Peltier thermoelectric cooling (TEC) effect, such as in small refrigerator devices used for camping and outdoor activities, automotive climate control seats, and localized cooling at the hot spots of chips. **Figure 6** gives an overview of the present and potential applications of thermoelectric generators (TEGs) [27]. Indeed, TEGs have been used for the power in miniaturized autarkic sensor systems, automotive waste heat recovery systems, ventilated wood stove, heating systems, water boilers, and heat recovery in industry.
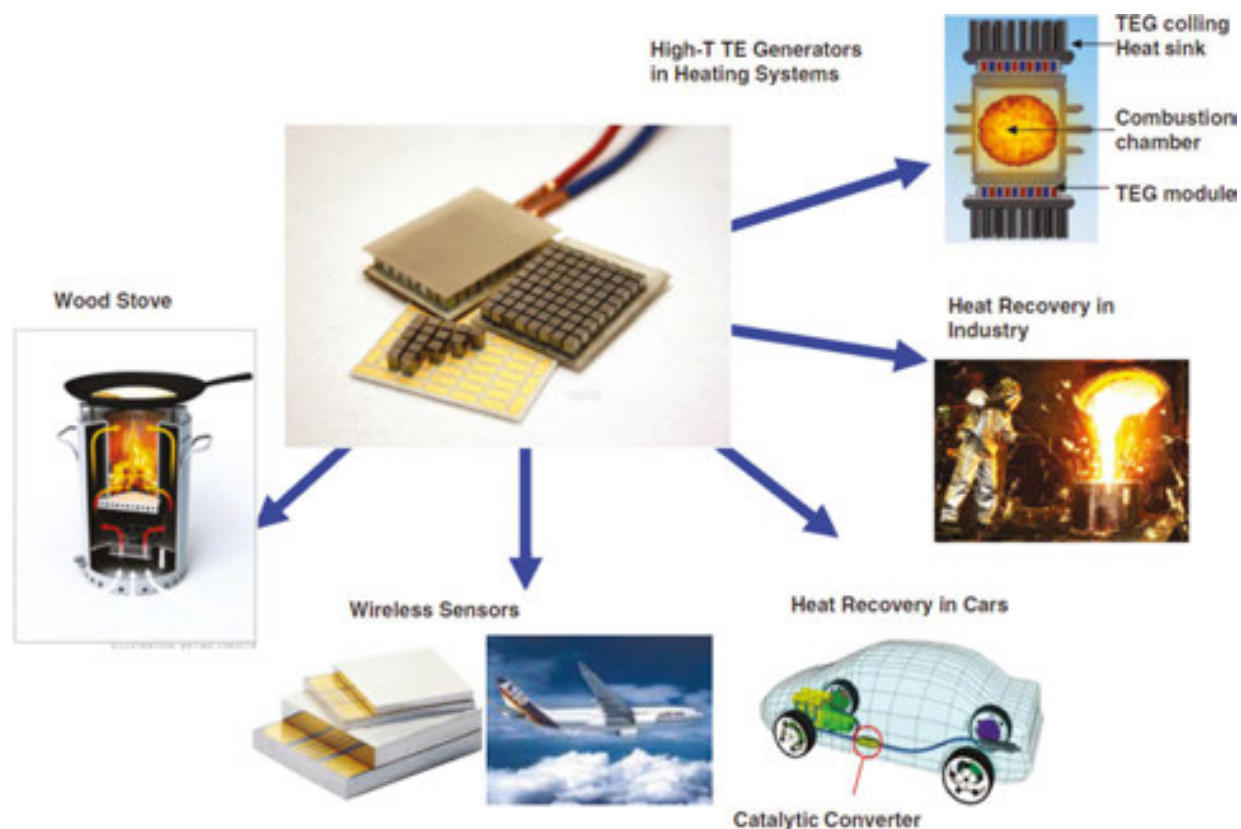
Figure 6. Overview of the potential applications of thermoelectric generators [27].

3.3. Thermoelectric properties of polycrystalline Bi_2Te_3, Bi_2Se_3, and Bi_3Se_2Te thin films with controlled structure morphology

Some typical HRTEM images of Bi_2Te_3, Bi_2Se_3, and Bi_3Se_2Te grown using PLD are shown in **Figure 7** [14–16]. HRTEM images performed on a high μ Bi_2Te_3 film with nanodisk-like morphology grown at 220°C are shown in **Figure 7a**. Clearly, the lower inset in **Figure 7a** shows the film with uniform thickness of approximately 295 nm and a SiO_2 layer with a thickness of 300 nm. It shows that projected period of 0.508 nm along the c-axis corresponds to the lattice spacing of the (0 0 6) planes. The highly (0 0 1)-orientated and crystallized structures of the film should facilitate the transport of charge carriers. The c-axis lattice constant of the Bi_2Te_3 film is 30.48 Å, which agrees closely with the value (30.44 Å) presented in JCPDS 82-0358. The other Bi_2Te_3 films grown at $T_S \geq 220$°C also display similar HRTEM results.

For a Bi_2Se_3 film deposited at 300°C and 40 Pa, an HRTEM image taken at the boundary of three platelets (P1, P2, and P3) revealed the granular-polycrystalline structure of the films (**Figure 7b**). Moreover, P1 and P2 partly overlapped and the corresponding fast Fourier transform (FFT) of this overlapping region indexed by {0 0 3} patterns of [0 1 0] zone axis was performed from the dashed-square area (**Figure 7b**, inset). The projected period along the c-axes of both P1 and P2 was 9.60 Å, corresponding to (0 0 3) planes, which was close to the reported value of 9.55 Å in Ref. [28].

HRTEM images of a Bi_3Se_2Te film deposited at 250°C and 40 Pa are shown in **Figure 7c** and **d**. Nanocrystallites with sizes of 10–20 nm are clearly observed in **Figure 7c**, confirming the nanocrystalline type of the Bi_3Se_2Te films. The interplanar spacing of the Bi_3Se_2Te (0 0 5) planes in the nanocrystallites is approximately 0.464 nm. Therefore, the *c*-axis lattice constant is determined to be 23.2 Å, closely agreeing with the value of 23.25 Å for Bi_3Se_2Te bulk (JCPDS 00-053-1190). In addition, the white lines in **Figure 7c** indicate the orientations of the (0 0 5) planes. It is seen that the overall orientation of the crystallites is disorganized. Intriguingly, near the interface of the film and substrate, the film has some nanoinclusions with sizes of 12–17 nm, as shown in **Figure 7d**. The EDS analysis shows that these are Bi semimetal nanoprecipitates (the inset in **Figure 7d**). The lattice spacing of Bi nanoinclusions is ~0.32 nm, corresponding to the Bi (0 1 2) planes. It has been found that Bi nanoinclusions can lead to the enhanced Seebeck coefficient and reduced lattice thermal conductivity owing to the low-energy electron filtering and phonon scattering at the nanoinclusions, respectively [29–31].
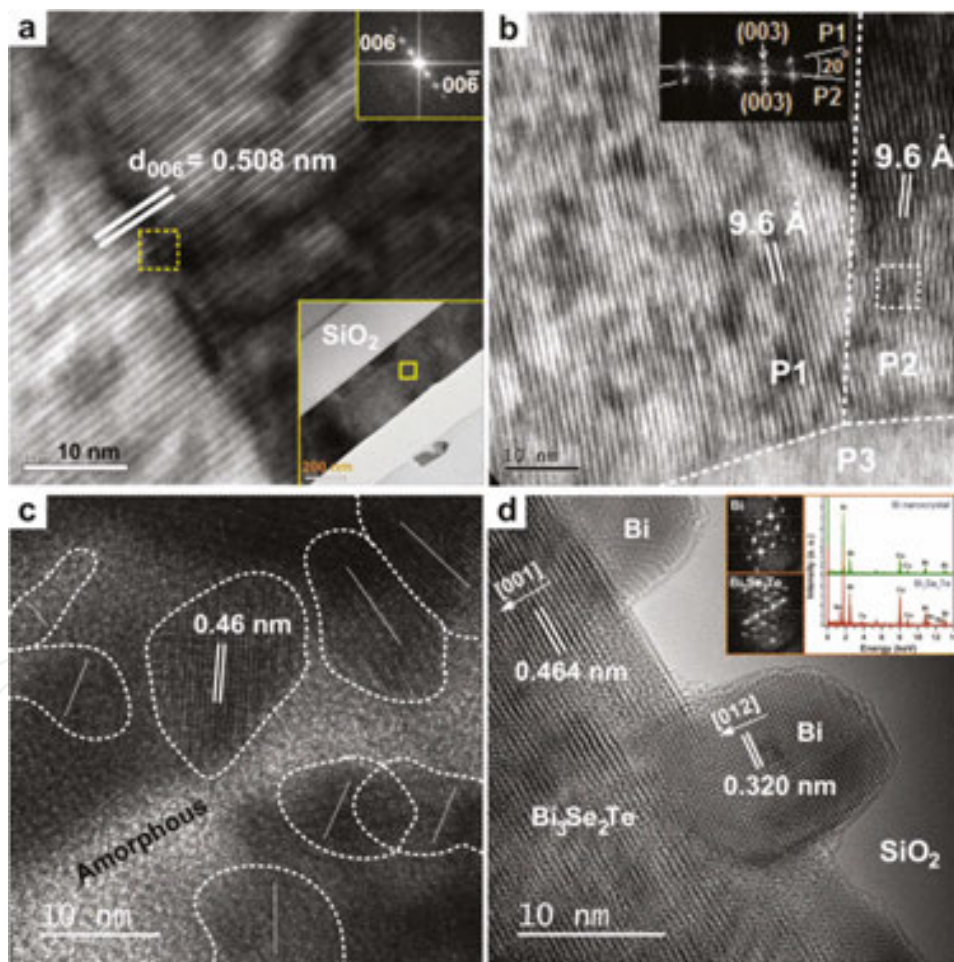

Figure 7. (a) HRTEM images of a high carrier mobility (μ) Bi_2Te_3 film with nanodisk-like morphology grown at 220°C and P_{Ar} of 80 Pa. (b) HRTEM image of an optimized Bi_2Se_3 film deposited at 300°C and P_{He} of 40 Pa. The inset shows the FFT patterns of the dashed-square area in the HRTEM image. (c and d) HRTEM images of the Bi_3Se_2Te film grown at 250°C and P_{He} of 40 Pa. The white lines in (c) indicate the (0 0 5)-orientation of nanograins. Inset in (d): FFT patterns and EDS spectra performed at film and Bi nanoinclusion positions.

Figure 8a shows the T_S-dependent α, σ, and PF (= $\alpha^2\sigma$) of some nanostructured Bi_2Te_3 films [15]. The σ value gradually increased from 34.5 ± 0.1 to 814.3 ± 1.5 S/cm when T_S was increased from 30 to 300°C, and then sharply decreased to 647.3 ± 0.4 S/cm at 340°C and 414.0 ± 1.2 S/cm at 380°C. The enhanced σ (= $647.3 - 814.3$ S/cm) of the films grown at 220–340°C originated from the substantially enhanced μ because the n exhibited a slight decrease [15]. Although the coupled relationship between σ (= $ne\mu$) and $|\alpha|$ (~$n^{-2/3}$) generally constrains the concurrent enhancement of σ and $|\alpha|$, a reduction in n and a substantial increase in μ in the same optimal range of T_S (= 220–340°C) could lead to high values of both σ and $|\alpha|$. Consequently, the PF of the stoichiometric Bi_2Te_3 films grown in the range of 220–340°C reached remarkably high values, ranging between 18.2 ± 0.25 and 24.3 ± 0.44 $\mu W\ cm^{-1}\ K^{-2}$, whereas the PF was low (≤ 0.44 $\mu W\ cm^{-1}\ K^{-2}$) in the case of nonstoichiometric films deposited at $T_S \leq 120$ or 380°C (**Figure 8a**).

Figure 8. (a) Substrate temperature (T_S) dependence of room temperature Seebeck coefficient α (red circles), electrical conductivity σ (blue triangulars), and power factor ($PF = \alpha^2\sigma$, black squares) of the Bi_2Te_3 and Bi_4Te_5 (for "PH" point) films. The morphology abbreviations: CNP, columnar nanoparticle; CNF, columnar nanoflower; ND, nanodisk; CP, compact polycrystalline; LTP, layered triangular platelet; PH, polyhedral. (b) Contour plot of the Bi_2Se_3 film's PF as a function of P_{He} and T_S. The morphology abbreviations: SC, smooth and compact; RG, rice grain; TP, triangular polygonal; S-LFs, super-layered flakes; L-HPs, layered hexagonal platelets. (c) Contour plot of the film's PF as a function of T_S from 200 to 350°C and P_{He} from 0.027 to 86.7 Pa. (d) $|S|$ vs. σ of the films in this study and the relevant novel TE materials in the literature, listed in **Table 1**. Solid curves denote different PFs from 1 to 50 $\mu W\ cm^{-1}\ K^{-2}$.

In order to check the evolution of the PF (= $\alpha^2\sigma$) as a function of P_{He} and T_S, the contour plot is illustrated **Figure 8b**. The PF of Bi_2Se_3 films increased with increasing T_S from 200 to 300°C because σ became considerably larger but the Seebeck coefficient diminished only slightly. However, for films deposited at 350°C, PF was lowered primarily because of the reduction in

S and not the increase in σ. At intermediate pressures (40–93 Pa), the Bi_2Se_3 films remained stoichiometric or slightly Se-rich compositions, which in turn led to the reduced carrier concentrations and significantly enhanced the α values [14]. Thus, the PF of Bi_2Se_3 films grown at intermediate pressure was typically higher than the PF of films grown at a low or high pressure. The optimal value of PF was $5.54 \pm 0.34\ \mu W\ cm^{-1}\ K^{-2}$ for the layered hexagonal platelet Bi_2Se_3 films deposited at 300°C and 40 Pa [14].

System	Type	Method	n (10^{19} cm^{-3})	μ (cm^2/Vs)	σ (S/cm)	α ($\mu V/K$)	PF (μW cm^{-1} K^{-2})	References
Bi_2Te_3	Layered smooth film	PLD	10.1	90.6	1464	−186	50.6	[39]
Bi_2Te_3	Layered compact polycrystalline	PLD	5.0	102	814.3	−172.8	24.3	[15]
Bi_2Te_3	Nanoparticle film	PLD	9.7	14.8	230	−91	1.9	[34]
Bi_2Te_3	Super-assembled film	PLD	4.0	12.4	79	−113	1.0	[33]
Bi_2Se_3	Layered hexagonal platelets	PLD	7.4	81.4	963.8	−75.8	5.5	[14]
Bi_3Se_2Te	Nanocrystalline film	PLD	35.5	34.4	1747.5	−68.8	8.3	[16]
Bi_2Te_3	Layered structure	Sputtering	95	12.1	1840	−70	8.8	[35]
Bi_2Se_3	Bulk	Melting and hot-pressing	–	–	251.9	−175	7.7	[32]
$Bi_2Se_{0.3}Te_{2.7}$	Bulk	Ball milling hot pressing	–	–	892	−190	32.2	[36]
$Bi_2Se_{1.5}Te_{1.5}$	Bulk	Zone melting	1.2	230	441.6	−193	16.5	[37]
$Bi_2Se_{1.8}Te_{1.2}$	Nanoplatelet bulk	Polyol method	–	–	199.6	−80.9	1.3	[38]
Bi_2Se_2Te	Bulk	Ball milling hot pressing	–	–	1613	−60	5.8	[36]

Table 1. Material, type, method, carrier concentration (n), mobility (μ), electrical conductivity (σ), Seebeck coefficient (S), power factor ($PF = S^2\sigma$) of the optimal bismuth chalcogenide films in this study as compared to properties of Bi_2Te_3, Bi_2Se_3, $Bi_2Se_xTe_{1-x}$ bulk and films reported in the literature. All the selected values were recorded at room temperature.

The T_S- and P_{He}-dependent PF of nanocrystalline Bi_3Se_2Te films is further shown in **Figure 8c**. The films grown at 200°C only have PFs of 1.0–2.8 $\mu W\ cm^{-1}\ K^{-2}$. The PFs of the films grown at higher T_S are significantly enhanced because of their high σ values. Around T_S = 250–350°C and P_{He} = 40 Pa, a window for high PF is clearly observed. An optimal PF of 8.3 $\mu W\ cm^{-1}\ K^{-2}$ is achieved for a Bi_3Se_2Te film deposited at 250°C and 40 Pa.

Table 1 summarizes the transport and room-temperature TE properties of bismuth chalcogenides in the literature [14, 15, 32–39]. For PLD growths, the highly (0 0 1)-oriented layered Bi_2Te_3 films achieved a PF of 50.6 $\mu W\ cm^{-1}\ K^{-2}$ [39], and the layered compact polycrystalline

film possessed a *PF* value of 24.3 μW cm^{-1} K^{-2} [15]. The Bi$_2$Se$_3$ films generally have lower TE properties than those of Bi$_2$Te$_3$ films. For example, the optimal *PF* of the Bi$_2$Se$_3$ films grown by PLD was 5.5 μW cm^{-1} K^{-2} [14], which was slightly lower than the *PF* of Bi$_2$Se$_3$ bulk (*PF* $\approx$ 7.7 μW cm^{-1} K^{-2}) [32]. The nanocrystalline Bi$_3$Se$_2$Te films had an optimal *PF* of 8.3 μW cm^{-1} K^{-2} [16]. Further, PLD growth allows fabrication of nanostructured TE films with different morphologies of nanoparticle Bi$_2$Te$_3$ film (*PF* = 1.9 μW cm^{-1} K^{-2}) [34] and super-assembled Bi$_2$Te$_3$ film (*PF* = 1.0 μW cm^{-1} K^{-2}) [33]. The Bi$_2$Te$_3$ film deposited by the sputtering technique had *PF* of 8.8 μW cm^{-1} K^{-2} [35]. There are some reports of TE properties for bulk materials of bismuth chalcogenides, such as Bi$_2$Se$_{1.8}$Te$_{1.2}$ nanoplatelet (*PF* $\approx$ 1.3 μW cm^{-1} K^{-2}) [38], Bi$_2$Se$_2$Te (*PF* $\approx$ 5.8 μW cm^{-1} K^{-2}), Bi$_2$Se$_{1.5}$Te$_{1.5}$ (*PF* $\approx$ 16.5 μW cm^{-1} K^{-2}) [37], and Bi$_2$Se$_{0.3}$Te$_{2.7}$ (*PF* $\approx$ 32.2 μW cm^{-1} K^{-2}) [36]. Unfortunately, the thermal conductivity κ of the films is missed in the reports to fully evaluate the TE performance of the films. Nevertheless, the κ of polycrystalline films with small grain sizes should be reduced thanks to the extensive phonon scattering at interfaces and grain boundaries.

Finally, **Figure 8d** shows the $|S|$ vs. σ plot for the list in **Table 1**. The solid curves denote different values of *PF*s (= $S^2\sigma$). It can be found that TE nanomaterials usually possess low σ values due to the separating or voided structure morphology, but bulk and thin films have superior σ. Note, the significant reduction in thermal conductivity κ is the key factor for employing nanostructured materials in the TE field.

4. Nanomechanical properties of Bi$_2$Te$_3$ and Bi$_3$Se$_2$Te thin films

Effects of helium ambient pressure (in PLD) on the nanomechanical properties of Bi$_2$Te$_3$ and Bi$_3$Se$_2$Te thin films have been investigated [9, 40]. The Bi$_2$Te$_3$ thin films were grown at T_S of 250°C on c-plane sapphire substrates using excimer laser PLD with a power density of 5 J/cm^2, at a repetition rate of 2 Hz. The helium pressures in PLD growth varied from 2 × 10^{-5} to 6.5 × 10^{-3} Torr. Similarly, Bi$_3$Se$_2$Te thin films were deposited on Al$_2$O$_3$ (0 0 0 1) substrates at a fixed substrate temperature of 250°C and P_{He} ranging from 2 × 10^{-5} to 6.5 × 10^{-1} Torr through PLD. The light source of the PLD system was a KrF excimer laser with λ = 248 nm, pulse duration of 20 ns, fluence of 7.0 J/cm^2, and repetition rate of 2 Hz. The target-to-substrate distance, the number of laser pulses and deposition time were 40 mm, 3000, and 25 min, respectively. The grown films had the average thickness of 200 nm (the average growth rate was ~0.67 Å/pulse). Nanoindentation experiments were performed on a MTS Nano Indenter® XP system with a three-sided pyramidal Berkovich indenter tip using the continuous stiffness measurement (CSM) technique [41]. The hardness and Young's modulus of the Bi$_2$Te$_3$ and Bi$_3$Se$_2$Te thin films were determined from the load-displacement results through the analytical method proposed by Oliver and Pharr [42].

As shown in **Figure 9a**, the hardness monotonically increased from 2.92 ± 0.12 to 4.02 ± 0.14 GPa for Bi$_2$Te$_3$ films, and from 2.5 ± 0.2 to 3.0 ± 0.1 GPa for Bi$_3$Se$_2$Te films when P_{He} was increased from 2.0 × 10^{-5} to 2.0 × 10^{-3} Torr. Similarly, the Young's modulus of Bi$_2$Te$_3$ thin films was 106.31 ± 0.63, 115.51 ± 1.92, and 127.46 ± 9.21 GPa for P_{He} at 2.0 × 10^{-5}, 2.0 × 10^{-4}, and 2.0 × 10^{-3} Torr,

respectively. For $P_{He} > 2.0 \times 10^{-3}$ Torr, the hardness (Young's modulus) of Bi_3Se_2Te films continues to increase with increasing P_{He}, namely 3.2 ± 0.1 GPa (105.2 ± 10.2 GPa) at 2.0×10^{-1} Torr and 5.8 ± 0.2 GPa (188.5 ± 4.3 GPa) at 6.5×10^{-1} Torr (**Figure 9b**).

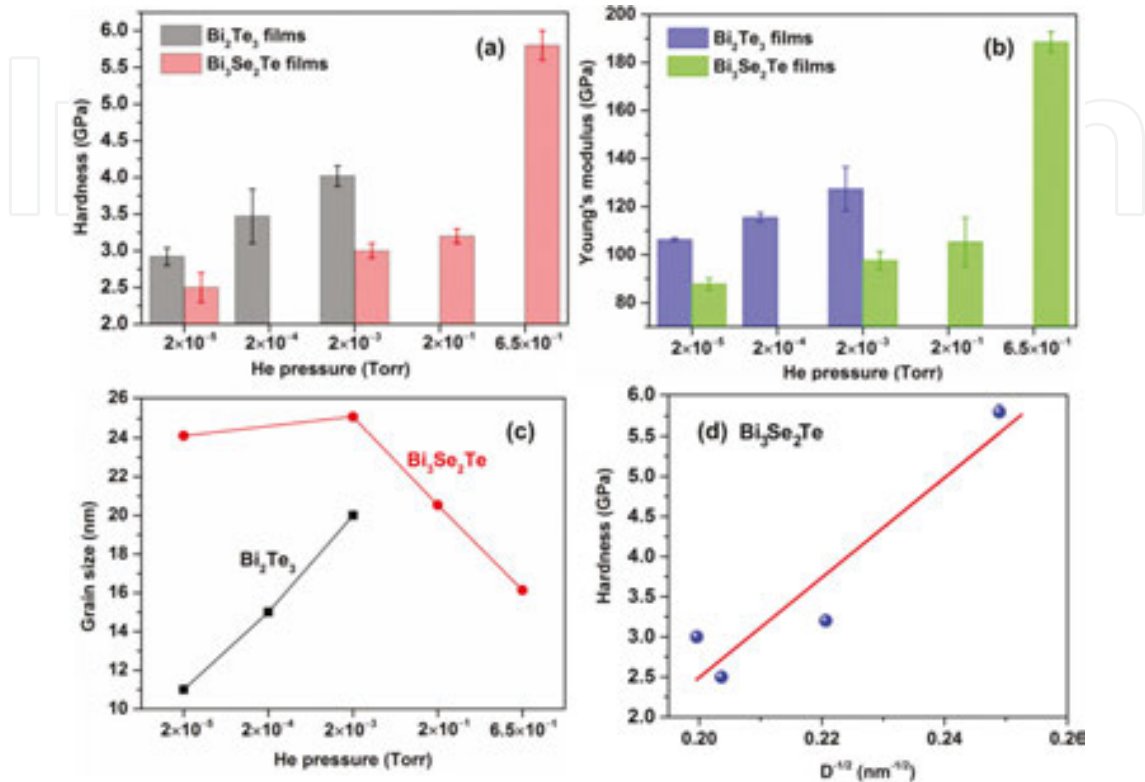**Figure 9.** Material and nanomechanical properties of Bi_2Te_3 and Bi_3Se_2Te thin films grown on Al_2O_3 (0 0 0 1) substrates at T_S of 250°C and various helium pressures (P_{He}) between 2.0×10^{-5} and 6.5×10^{-1} Torr [9, 40]: (a and b) the hardness and Young's modulus, (c) grain size (*D*), (d) the Hall-Petch behavior observed on the Bi_3Se_2Te thin films, in which the hardness is observed to increase approximately with $D^{-1/2}$ (*D* is grain size).

The crystallite sizes (*D*) of the films were estimated using the Scherrer equation $D = 0.9\lambda/Bcos\theta$, where λ, *B*, and θ are the X-ray wavelength, full width at the half maximum of the Bi_2Te_3 (0 0 15) peak or Bi_3Se_2Te (0 0 5) peak, and Bragg diffraction angle, respectively. The P_{He}-dependent *D* of the Bi_2Te_3 and Bi_3Se_2Te films is shown in **Figure 9c**. The grain size increases monotonically from 11.0 to 20.0 nm for Bi_2Te_3 and from 16.1 to 20.5 nm for Bi_3Se_2Te with increasing P_{He} from 2.0×10^{-5} to 2.0×10^{-3} Torr. In the nanoscale, grain size can affect significantly the mechanical properties of materials. The dislocation activities can be drastically suppressed in a polycrystalline material when the grain size is decreased, and thus the grain boundary sliding and/or grain rotations become the dominant deformation behavior, which in turn would lead to the manifestations of the inverse Hall-Petch effect [43]. Softening caused by grain boundary sliding is mainly attributed to large amount of defects in grain boundaries, which allow rapid diffusion of atoms and vacancies under stress [44]. Consequently, the plastic deformation of Bi_2Te_3 films should be dominated by the grain boundary sliding and/or grain rotation rather than the dislocation activity because of $D \leq 20$ nm [40], which is consistent with the results in Refs. [45–48].

In contrast, the 200-nm-thick Bi_3Se_2Te films with D of 16.1–25.1 nm grown at a larger P_{He} range of 2.0×10^{-5} to 6.5×10^{-1} Torr exhibited the nanomechanical followed Hall-Petch relationship [44, 49]. The hardness and Young's modulus of the Bi_3Se_2Te thin films monotonically increased with increasing P_{He} because of a corresponding decrease in grain sizes (**Figure 9a–c**). **Figure 9d** shows that hardness (H) increased linearly with $D^{-1/2}$ (where D is the grain size of the Bi_3Se_2Te films in the nanoscale regime) which is the typical Hall-Petch relationship [44, 49]. This is because the multiplication and mobility of dislocations are hindered by reducing the grain size [44]. It is reasonable for the observed phenomenon when the present grain sizes ranged between 25.1 and 16.1 nm which is larger than the typical critical D_c of 10 nm [44, 49]. It is demonstrated that the hardness and Young's modulus of the Bi_2Te_3 and Bi_3Se_2Te thin films can be enhanced by proper selection of the ambient pressure in PLD growths.

5. Topological insulator bismuth chalcogenide thin films and their novel properties

5.1. The epitaxial growths of bismuth chalcogenide thin films

Topological insulator (TI), a new class of quantum matter, possesses insulating in bulk and robust gapless topological surface states (TSSs) in which the spin of the electron is locked perpendicular to its momentum by strong spin-orbit interaction [6, 50, 51]. TIs have been identified as promising materials for exploiting exciting physics and developing potential applications in optoelectronics, spintronics, and quantum computations [50–54]. Dirac fermions in TIs have also been studied by angle-resolved photoemission spectroscopy [55–57] or scanning tunneling microscopy [58, 59]. In magnetotransport studies, TSS can be studied by weak antilocalization (WAL) [4, 9, 60, 61] and Shubnikov-de Haas oscillations [3, 62].

Topological insulator bismuth chalcogenide thin films have been grown epitaxially on various substrates using PLD. Onose et al. reported the epitaxial growth of Bi_2Se_3 thin films on InP (1 1 1) substrates (the lattice mismatch of 0.2%) [7]. A designed Se-rich target with an atomic ratio of Bi:Se = 2:8 was used to compensate for the issue of high doping carriers and to avoid unwanted Se-deficient phases. The pulsed laser power and repetition were 140 mJ and 10–20 Hz, respectively. The Bi_2Se_3 films obtained a small full-width at half-maximum (FWHM) for the XRD rocking curve of (0 0 0 6) peak. The surfaces of the films are composed of triangular pyramids with step-and-terrace structures, reflecting the hexagonal symmetry of Bi_2Se_3. The epitaxial relationship is Bi_2Se_3 (0 0 1) ∥ InP (1 1 1) and Bi_2Se_3 [1 1 $\bar{2}$ 0]∥InP [0 0 $\bar{1}$]. Le et al. reported the epitaxial growth of Bi_2Se_3 films on $SrTiO_3$ (STO) (1 1 1) substrates using PLD at T_S of 300 and 350°C [63]. The PLD conditions were the pulse fluence of 3.7 J/cm^2, helium pressure of 40 Pa (300 mTorr), and repetition rate of 2 Hz. The laser source was KrF excimer laser (λ = 248 nm, duration 20 ns). By comparing the Bi_2Se_3 {0 1 5} and STO {2 0 0} diffraction peaks, the epitaxial relationship between the film and substrate was determined to be Bi_2Se_3 (0 0 1) ∥ STO (1 1 1) and Bi_2Se_3 [1 1 0] ∥ STO [$\bar{1}$ 1 0] [63].

Figure 10 presents the PLD epitaxial growths of Bi_2Te_3, Bi_2Se_3, and Bi_3Se_2Te thin films on large-misfit substrates [9, 53, 64]. The PLD conditions for growing Bi_2Te_3 films on STO (1 0 0) were as follows: substrate temperature of 300°C; helium ambient pressure of 40 Pa; repetition rate of 2 Hz; pulsed fluence of approximately 3.4 J/cm². As shown in **Figure 10a**, a ϕ-scan was conducted on the (0 1 5) plane of a 200-nm-thick Bi_2Te_3 film and the (1 1 1) plane of an STO (1 0 0) substrate in skew symmetric geometry by tilting the samples. The in-plane orientation of a hexagonal h-Bi_2Te_3/STO (1 0 0) film displayed a 12-fold symmetry instead of the expected six-
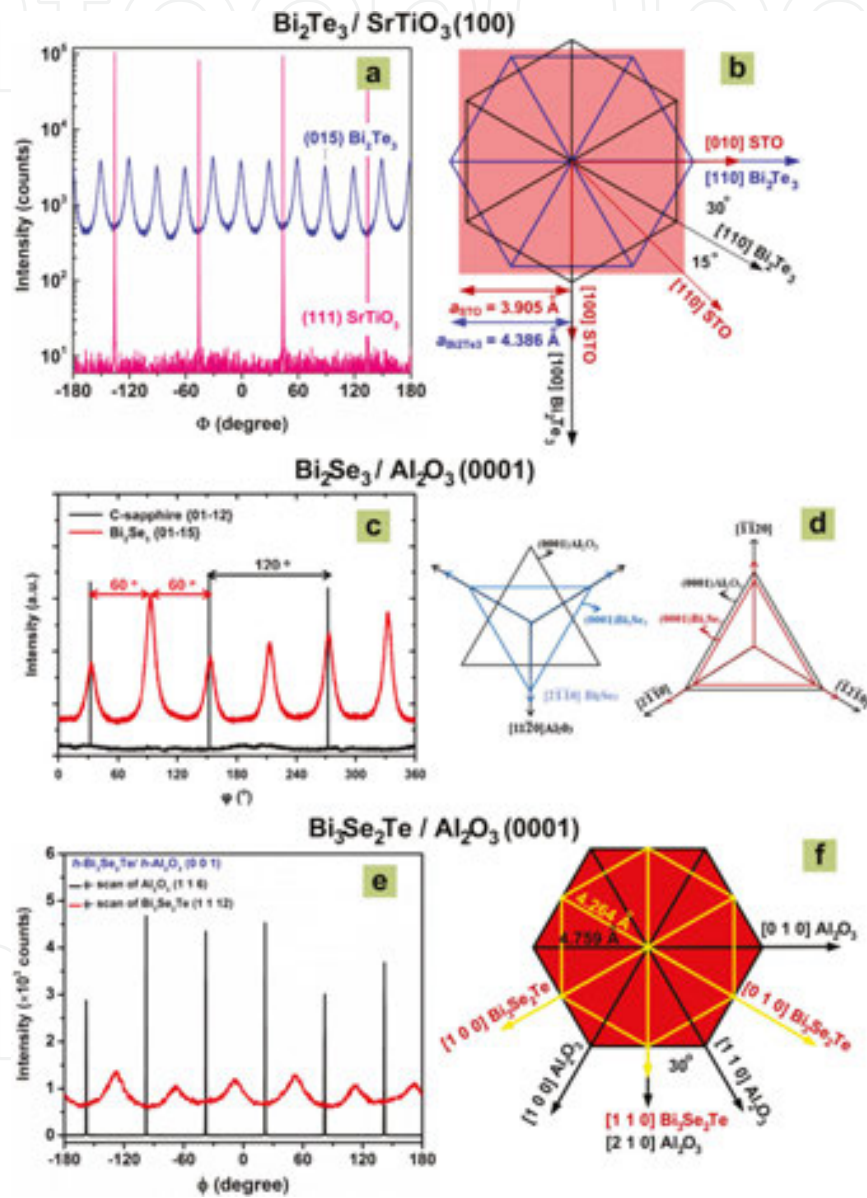

Figure 10. Bi_2Te_3 films grown on $SrTiO_3$ (1 0 0) substrates [53]: (a) XRD ϕ-scan patterns of the 200-nm-thick Bi_2Te_3 (0 1 5) plane and the $SrTiO_3$ (1 1 1) plane; (b) schematics of the in-plane arrangement of h-Bi_2Te_3 / $SrTiO_3$ (1 0 0). Bi_2Se_3 films grown on c-plane sapphire substrates [64]; (c) in-plane ϕ-scan $\{0\,1\,\bar{1}\,5\}$ planes of the film and $\{0\,1\,\bar{1}\,2\}$ planes of the substrate; (d) the schematic depicting twin/domain growth: in one case, the basal plane of Bi_2Se_3 is aligned with that of Al_2O_3, and in the other, there is a rotation of 60°/180°. Bi_3Se_2Te films grown on c-plane sapphire substrates [9]; (e) ϕ-scan patterns of hexagonal h-Bi_3Se_2Te thin films grown on Al_2O_3 (0 0 0 1) substrates; and (f) schematics of the in-plane arrangement of hexagonal h-Bi_3Se_2Te/h-Al_2O_3 (0 0 0 1).

fold symmetry of the (0 1 5) plane in Bi_2Te_3. **Figure 10b** shows a schematic drawing of the in-plane atomic arrangement between an h-Bi_2Te_3 film and an STO (1 0 0) substrate. Since the principal crystallographic orientations of h-Bi_2Te_3 films grown on STO (1 0 0) substrates can be aligned along either the STO [1 0 0] or STO [0 1 0] directions, the in-plane arrangements result in an observed 12-fold symmetry. The angle differences between STO [0 1 0] and the two orientations of h-Bi_2Te_3 [1 1 0] were 30° and 0°, respectively, as shown in **Figure 10b**. In other words, the in-plane relationships were Bi_2Te_3 [1 1 0] ‖ STO [0 1 0] and Bi_2Te_3 [1 0 0] ‖ STO [1 0 0]. Lee et al. reported epitaxial growth via domain matching epitaxy of Bi_2Se_3 thin films on Al_2O_3 (0 0 0 1) substrates with over 13% lattice misfit and a critical thickness of less than one monolayer [64]. A relatively low repetition rate of 0.2 Hz and low T_S of 250°C are key parameters of the PLD growth to achieving high-quality Bi_2Se_3 epitaxial films. **Figure 10c** shows ϕ-scan XRD results performed on $\{0\ 1\ \overline{1}\ 5\}$ planes of the film and $\{0\ 1\ \overline{1}\ 2\}$ planes of the substrate. Clearly, the presence of six peaks corresponding to the Bi_2Se_3 $\{0\ 1\ \overline{1}\ 5\}$ planes confirmed the epitaxy. A schematic depicting twin/domain growth and direction in the study is illustrated in **Figure 10d** [64]. In one case, the Bi_2Se_3 basal plane is aligned with that of Al_2O_3, and in the other, there is a rotation of 60°/180°. The epitaxial relationships are written as (0 0 0 1) Bi_2Se_3 ‖ (0 0 0 1) Al_2O_3 (out-of-plane) and [2 $\overline{1}$ $\overline{1}$ 0] Bi_2Se_3 ‖ [2 $\overline{1}$ $\overline{1}$ 0] Al_2O_3 or [2 $\overline{1}$ $\overline{1}$ 0] Bi_2Se_3 ‖ [1 1 $\overline{2}$ 0] Al_2O_3 (in-plane). **Figure 10e** shows the typical ϕ-scan patterns of hexagonal h-Bi_3Se_2Te/h-Al_2O_3 (0 0 0 1) [9]. With the skew symmetric geometry, the ϕ-scan measurements were performed on the (1 1 6) plane of Al_2O_3 substrates and the (1 1 12) plane of Bi_3Se_2Te films. As shown in **Figure 10e**, the in-plane orientations of both Al_2O_3 (1 1 6) and Bi_3Se_2Te (1 1 12) exhibited six-fold symmetries with a 30° difference. **Figure 10f** illustrates the in-plane atomic arrangement between h-Bi_3Se_2Te and h-Al_2O_3 (0 0 0 1). The epitaxial relationship between the films and substrates is (0 0 0 1) Bi_3Se_2Te ‖ (0 0 0 1) Al_2O_3 and [1 1 0] Bi_3Se_2Te ‖ [2 1 0] Al_2O_3 [9]. This in-plane orientation was established to obtain the optimal lattice matching.

5.2. Magnetotransport properties of bismuth chalcogenide thin films

The weak antilocalization (WAL) which is a negative quantum correction to classical MR caused by the wave nature of electrons is used as a signature of TSS. In TIs, WAL is induced by both the helicity of the surface state and the spin-orbit coupling of bulk [4, 61, 65, 66]. In a low B field, the 2D WAL MR of a system with strong spin-orbit interaction can be described using the Hikami-Larkin-Nagaoka model [65], which is [4, 60, 61]

$$\frac{\Delta R_W(B)}{[R_W(0)]^2} = -\alpha\frac{e^2}{2\pi^2\hbar}\left[\Psi\left(\frac{1}{2}+\frac{B_\phi}{B}\right)-\ln\left(\frac{B_\phi}{B}\right)\right] \tag{8}$$

where R_W is the sheet resistance, $\Delta R_W = R_W(B) - R_W(0)$, $\Psi(x)$ is the digamma function, $B_\phi = \hbar/(4eL_\phi^2)$ is a magnetic field varying with the coherence length L_ϕ, α is a parameter and reflects the number of conduction channels. In a 3D TI, $\alpha = -1/2$ for a single coherent transport

channel in the 2D surface states, and $\alpha = -1$ for two independent coherent transport channels with similar L_ϕ in the 2D surface states [60, 65].

The typical magnetoresistance (MR) results of some bismuth chalcogenides (i.e., Bi_2Te_3, Bi_2Se_3, and Bi_3Se_2Te) thin films grown by PLD are presented in **Figure 11** [9, 64, 67]. The Bi_2Te_3, Bi_2Se_3,

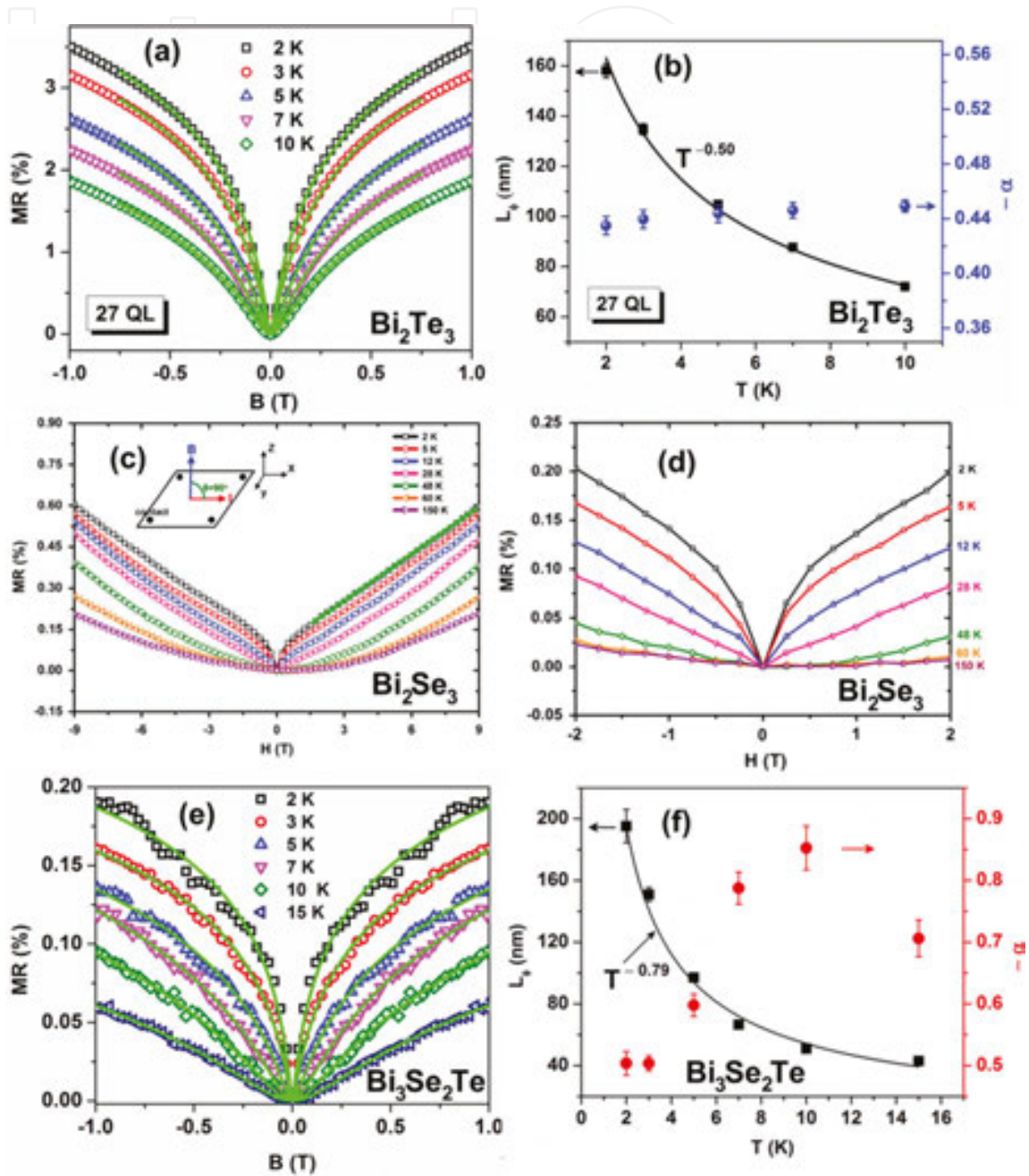**Figure 11.** Magnetoresistance (MR) results of the Bi_2Te_3, Bi_2Se_3, and Bi_3Se_2Te thin films grown by PLD [9, 64, 67]. (a and e) The MR ($B = \pm1$ T) of a 27-nm-thick Bi_2Te_3 and a 200-nm-thick Bi_3Se_2Te films grown on Al_2O_3 (0 0 0 1) substrates. (b and f) Variation in the extracted electron dephasing length L_ϕ and parameter $-\alpha$ of the films as a function of temperatures. (c and d) MR of the epitaxial Bi_2Se_3 films grown on Al_2O_3 (0 0 0 1) substrates at $T_S = 250°C$ as a function of temperatures [64]. The solid green lines in (a) and (e) in low B are the theoretical predictions of 2D weak antilocalization (WAL) using Eq. (8).

and Bi_3Se_2Te thin films were grown on Al_2O_3 (0 0 0 1) substrates using PLD at T_S of 225, 250, and 250°C, respectively [9, 64, 67]. The WAL effect which presents as a sharp increase in resistance when B increases in the low magnetic field B regime is clearly observed on the films. **Figure 11a**, **b**, **e** and **f** show MR curves at several temperatures (T) and the extracted $\alpha(T)$ and $L_\phi(T)$ values using Eq. (8) for the 27-QL (~27 nm)-thick Bi_2Te_3 and 200-nm-thick Bi_3Se_2Te thin films [9, 67]. At 2 K, L_ϕ are 158.1 and 195.2 nm, and L_ϕ decreases monotonically with increasing T, obeying the power laws, as $L_\phi \sim T^{-0.50}$ and $L_\phi \sim T^{-0.79}$ for the Bi_2Te_3 and Bi_3Se_2Te films, respectively (**Figure 11b** and **f**). Theoretically, the result of $L_\phi \sim T^{-0.50}$ observed in the 27-QL-thick Bi_2Te_3 thin film indicates the predominant electron-electron scattering in 2D weakly disordered systems. The $L_\phi \sim T^{-0.79}$ is closed to the $L_\phi \sim T^{-0.75}$ for 3D systems, if e-e scattering is the dominant dephasing source [9]. The electron screening effect in 3D system is more effective than that in 2D systems. However, the e-e scattering is strongly weakened with high carrier densities ($n = 10^{20}$ cm^{-3} for the Bi_3Se_2Te films [9]). In 3D disordered conductors (namely, in the bulk state), dephasing by electron-phonon (e-ph) scattering would be significant and dominant. The e-ph scattering also causes a faster decay rate on L_ϕ, that is, $L_\phi \sim T^{-1.0}$ [68]. Additionally, the combination of 2D e-e scattering in the TSS thin layer and e-ph scattering in the bulk would further result in the $L_\phi \sim T^{-0.79}$. Consequently, e-ph scattering could be the force of channel separation as temperatures increase. It is worthy of mentioning that the MR result is a signature (not conclusive evidence) for the presence of TSS on Bi_3Se_2Te films. Further theoretical calculations and experiments are needed for reaching a final conclusion.

Figure 11b and **f** also present the $-\alpha(T)$ results of the Bi_2Te_3 and Bi_3Se_2Te films. The $-\alpha$ values of the Bi_2Te_3 film increase with increasing T from 0.43 at 2 K to 0.45 at 10 K, indicating the existence of a single coherent transport channel (i.e., likely a single surface state) [61]. Meanwhile, the $-\alpha$ values of the 200-nm-thick Bi_3Se_2Te film increase with increasing T from 0.5 at 2 K to 0.85 at 10 K and to 0.71 at 15 K, suggesting increased channel separation with T [69]. In WAL, the independent phase-coherent channels occur when the carriers in one channel lose phase coherence before being scattered into the other channel.

In **Figure 11c**, the MR (B,T) of a 50-nm-thick Bi_2Se_3 film was measured with B perpendicular to the film plane and ranging from −9 T to +9 T. At low B and T, the distinctive dips of WAL are clearly observed. The WAL effect results from strong spin-orbit coupling, showing the absence of backscattering giving rise to the destructive interference between the two time reversal symmetry loops when there is no magnetic field [64]. Resistance increases sharply with increasing B because the quantum interference is destroyed and backscattering increases (**Figure 11c**). **Figure 11d** is the enlarged MR at low B (−2 T to +2 T), and it reveals the existence of WAL as a function of T in a discernible way [64]. WAL gradually weakens as temperature increases, eventually disappearing entirely at T = 48 K; thus, the dependence on B is quadratic-like at low field. The MR cusp feature at low B is broadened and finally disappears with increasing temperature owing to the decrease in the phase coherence length. In addition to the WAL effect, **Figure 11c** shows a 2D, non-saturating linear MR at high B, which usually occurs with several TI materials of Bi_2Se_3 [70], Bi_2Te_3 [71], Bi_2Te_2Se [72], and Bi_3Se_2Te [9]. Theoretical models propose that the linear MR can appear in the gapless linear-dispersive energy spectrum when only the first landau level is filled [73, 74], or in the presence of both the gapless linear

spectrum and Landau level overlaps [75]. Noticeably, the WAL and linear MR simultaneously reflect the 3D contribution of spin-orbit coupling in bulk and the Dirac nature of the 2D surface states. Because the magneto transport is a bulk sensitive measurement, it remains a major challenge to directly probe the topological nature [64].

5.3. Proximity-induced superconductivities in Bi inclusions/bismuth chalcogenide thin films

Recent studies have shown a two-dimensional interface state between TIs and superconductors resulting from the superconducting proximity effect that supports Majorana fermions [76, 77]. Majorana fermions, novel particles which are their own antiparticles, can potentially be applied to topological quantum computing, which has motivated intense interest in TIs [53].
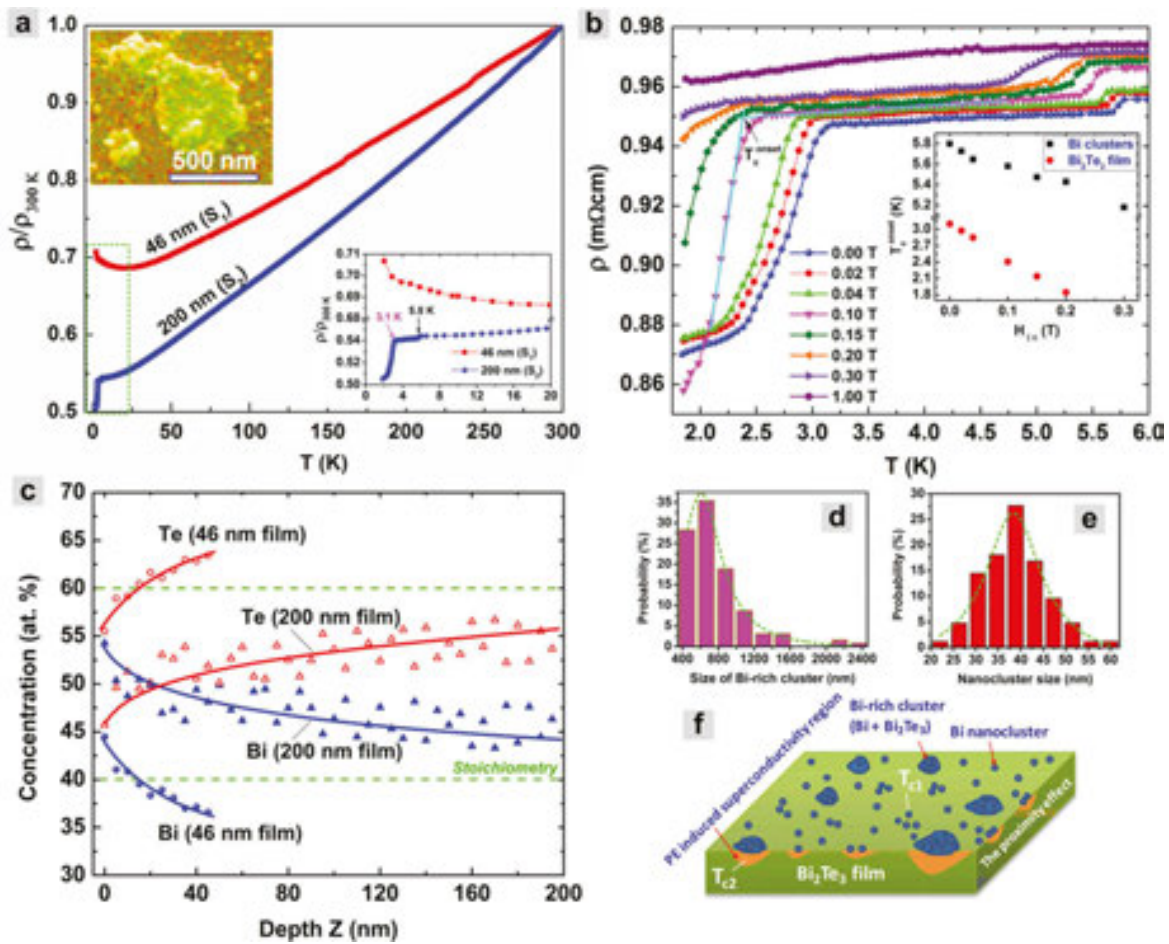

Figure 12. (a) Temperature-dependent normalized *ab* resistivities ($\rho/\rho_{300\ K}$) between 1.8 and 300 K of 46- and 200-nm-thick Bi_2Te_3 films. Upper inset: an EDS mapping image of a typical Bi-rich cluster. Lower inset: zoomed-in view of the $\rho/\rho_{300\ K}$ in the low temperature range. (b) $\rho(T)$ in 1.75–6.0 K of the 200 nm film at various $H_{||c}$ from 0 to 1 T. Inset: the onset T_c of the two superconducting transitions as a function of magnetic field. (c) Auger electron spectroscopy (AES) elemental depth profiling of a non-superconducting (46-nm-thick) and a superconducting (200-nm-thick) Bi_2Te_3 films. (d and e) The size distribution of Bi-rich clusters and Bi nanoclusters inside the clusters. (f) Schematics of the surface characteristics and a suggested superconducting mechanism in the Bi_2Te_3 films [53].

Koren et al. observed the local superconductivity in Bi_2Te_2Se and Bi_2Se_3 films below 2–3 K, which was naturally induced by small amounts of superconducting Bi inclusions or precipitations on the surface [78]. Moreover, Le et al. reported superconductivity at an onset critical temperature of approximately 3.1 K in a topological insulator 200-nm-thick Bi_2Te_3 thin film grown by pulsed laser deposition [53]. Indeed, **Figure 12a** shows the normalized resistivity $\rho/\rho_{300\,K}$ of a 46-nm-thick Bi_2Te_3 film (S_1) and a 200-nm-thick Bi_2Te_3 film (S_2) as functions of temperatures (T) from 1.8 to 300 K. Both films show a decrease in resistivity (ρ) with decreasing T in the range of 20–300 K, implying that the films exhibit weak metallic properties commonly seen in narrow band-gap semiconductors with high carrier concentrations [53]. Below 20 K (**Figure 12a**, the lower inset), the $\rho/\rho_{300\,K}$ of S_1 shows a gentle upturn because of the weak localization of electrons [7], whereas the $\rho/\rho_{300\,K}$ of S_2 reaches a plateau before dropping slightly at $T_{c1} \approx 5.8$ K and then sharply at $T_{c2} \approx 3.1$ K. **Figure 12b** further shows the $H_{||c}$-dependent $\rho(T)$ of S_2 in the low T regime, where $H_{||c}$ is the applied magnetic field along the c-axis of the film. At $H_{||c} = 0$, ρ drops abruptly by 8% below T_{c2}^{onset} but does not go down to zero, even at $T = 1.8$ K. This nonzero ρ at low T indicates that the superconducting volume ratio is not 100%. The inset in **Figure 12b** shows that the $T_{c2}^{onset}(T_{c1}^{onset})$ decreases from 3.1 (5.8) to 1.8 (5.4) K with increasing $H_{||c}$ from 0 to 0.2 T, strongly indicating that both transitions are superconducting in nature.

The detailed investigations of S_2 strongly suggest the existence of superconducting Bi nanoclusters on the surface that induce the $T_{c1} \sim 5.8$ K. EDS lateral elemental mapping revealed that the distributions of Te and Bi were not uniform, and many Bi-rich (47–54 at.%) clusters were visible (green color), as shown in the upper inset in **Figure 12a**, differing substantially from the uniform distribution and cluster-free surface observed in film S_1. The size distribution and the most probable size of Bi-rich clusters are in the range of 400–2400 nm and 560–772 nm, respectively. Intriguingly, a closer inspection reveals that Bi-rich clusters are composed by some Bi nanoclusters (or nanograins) with a size of 20–62 nm.

The Bi-rich environment on the film surface is confirmed by AES analysis (**Figure 12c**) [53]. This is because the vapor pressure of Te (at $T_S = 300°C$) is approximately 10^5 times higher than that of Bi, and therefore, more Te atoms are re-evaporated from the 300°C substrates [79]. The loss of Te is more severe in film S_2 than in film S_1 (14.3% in S_2 and 4.5% in S_1 at depth $Z = 0$, **Figure 12c**) because of the six times longer deposition time of S_2 (60 min) compared to S_1 (10 min). In addition, the nonstoichiometric effect is strongly depth-dependent (**Figure 12c**). The Te/Bi ratio gradually increases toward the stoichiometric ratio of 3/2 in 200-nm-thick films or slightly exceeds it (Te-rich) in 46-nm-thick films when the depth (Z) of the films increases. Under such a sufficiently high surface concentration of Bi atoms, the Bi clusters precipitate and segregate readily on the S_2 surface to minimize overall free energy, as long as the substrate temperature of 300°C is higher than the 271°C melting point of Bi, as demonstrated in **Figure 12f**. Notably, the Bi clusters can only be observed in highly Bi-rich (14.3% at $Z = 0$) films (S_2) and not in low Bi-rich (4.5% at $Z = 0$) films (S_1), suggesting a critical Bi-rich concentration for Bi precipitation (separating a Bi phase) in a Bi_2Te_3 film [53]. The T_{c1} at ~5.8 K found in our samples should be induced by the superconducting transition of the Bi nanoclusters, which is

closely consistent with the T_c of 6.3 K for the surface Bi islands observed in Bi_2Te_2Se films [78]. The tiny resistivity drop at T_{c1} = 5.8 K (by approximately 0.5%, **Figure 12b**) indicates that the amount of superconducting Bi nanoclusters in S_2 is likely small and, therefore, the Josephson coupling between these islands is extremely weak. Since the superconductivity of Bi nano-clusters survived until $H_{\|c}$ = 1.0 T (**Figure 12b**), the critical field of Bi nanoclusters is in between 0.3 and 1.0 T. This section demonstrates that natural defects generated during PLD growths, namely superconducting Bi nanoclusters or Bi inclusions, can substantially induce non-superconducting TI thin films (i.e., Bi_2Te_3, Bi_2Se_3, and Bi_2Te_2Se) into superconducting states at low temperatures.

6. Conclusion

This chapter provides the effects of ambient pressures and substrate temperatures in PLD growths on the structural-morphology, thermoelectric, nanomechanical, and magnetoresist-ance properties of bismuth chalcogenide thin films. The thermoelectric power factor of the stoichiometric Bi_2Te_3 films grown in the range of 220–340°C and P_{Ar} of 80 Pa reached remarkably high values, ranging between 18.2 ± 0.25 and 24.3 ± 0.44 μW cm^{-1} K^{-2}. The optimal PF values were 5.54 ± 0.34 μW cm^{-1} K^{-2} for the layered hexagonal platelet Bi_2Se_3 films deposited at 300°C and P_{He} of 40 Pa and 8.3 μW cm^{-1} K^{-2} for the nanocrystalline Bi_3Se_2Te films deposited at 250°C and P_{He} of 40 Pa. We also reported the effects of P_{He} in PLD on nanomechanical properties (i.e., hardness and Young's modulus) of Bi_2Te_3 and Bi_3Se_2Te thin films. It was observed that the hardness and Young's modulus increased with increasing P_{He}, depending on the grain sizes following the inverse Hall-Petch effect for Bi_2Te_3 films grown at $P_{He} \leq 2.0 \times 10^{-3}$ Torr and following the Hall-Petch relationship for Bi_3Se_2Te grown at P_{He} of 2.0×10^{-5} to 6.5×10^{-1} Torr. PLD has been successfully employed to grow epitaxially bismuth chalcogenide thin films on large-misfit substrates, for example, $Bi_2Te_3/SrTiO_3$ (1 0 0), Bi_2Se_3/Al_2O_3 (0 0 0 1), and Bi_3Se_2Te/Al_2O_3 (0 0 0 1). The magnetotransport studies show that the bismuth chalcogenide thin films such as Bi_2Te_3, Bi_2Se_3, and Bi_3Se_2Te films present a two-dimensional weak antilocalization effect in a low magnetic field (B) regime and linear magnetoresistance in a high B regime, which could be attributed to the topological insulator surface states. Furthermore, proximity-induced superconductivities in Bi_2Te_3 thin films have an onset T_c of approximately 3.1 K, evidently induced by Bi inclusions (nanoclusters with onset T_c at 5.8 K) segregated on the surface of films.

Author details

Phuoc Huu Le[1*] and Chih Wei Luo[2,3*]

*Address all correspondence to: lhuuphuoc@ctump.edu.vn and cwluo@mail.nctu.edu.tw

1 Faculty of Basic Sciences, Can Tho University of Medicine and Pharmacy, Can Tho, Vietnam

2 Department of Electrophysics, National Chiao Tung University, Hsinchu, Taiwan

3 Taiwan Consortium of Emergent Crystalline Materials, Ministry of Science and Technology, Taipei, Taiwan

References

[1] Venkatasubramanian R, Siivola E, Colpitts T, O'Quinn B. Thin-Film thermoelectric devices with high room-temperature figures of merit. Nature. 2001; 413: 597–602. doi: 10.1038/35098012

[2] Snyder GJ, Toberer ES. Complex thermoelectric materials. Nat. Mater. 2008; 7: 105–114. doi:10.1038/nmat2090

[3] Qu D-X, Hor YS, Xiong J, Cava RJ, Ong NP. Quantum oscillations and hall anomaly of surface states in the topological insulator Bi_2Te_3. Science. 2010; 329: 821–824. doi: 10.1126/science.1189792

[4] Bao L, He L, Meyer N, Kou X, Zhang P, Chen Z, Fedorov AV, Zou J, Riedemann TM, Lograsso TA, Wang KL, Tuttle G, Xiu F. Weak anti-localization and quantum oscillations of surface states in topological insulator Bi_2Se_2Te. Sci. Rep. 2012; 2: 726 (1–7). doi:10.1038/srep00726

[5] Hsieh D, Qian D, Wray L, Xia Y, Hor YS, Cava RJ, Hasan MZ. A topological Dirac insulator in a quantum spin Hall phase. Nature. 2008; 452: 970–974. doi:10.1038/nature06843

[6] Moore JE. The birth of topological insulators. Nature. 2010; 464: 194–198. doi:10.1038/nature08916

[7] Onose Y, Yoshimi R, Tsukazaki A, Yuan H, Hidaka T, Iwasa Y, Kawasaki M, Tokura Y. Pulsed laser deposition and ionic liquid gate control of epitaxial Bi_2Se_3 thin films. Appl. Phys. Express. 2011; 4: 083001. doi:10.1143/APEX.4.083001

[8] Zhang HB, Yu HL, Bao DH, Li SW, Wang CX, Yang GW. Weak localization bulk state in a topological insulator Bi_2Te_3 film. Phys. Rev. B. 2012; 86: 075102. doi:10.1103/PhysRevB.86.075102

[9]   Le PH, Chiu S-P, Jian S-R, Luo CW, Lin J-Y, Lin J-J, Wu KH, Gospodinov M. Nanome-chanical, structural, and transport properties of Bi_3Se_2Te thin films. J. Alloys Compd. 2016; 679: 350–357. doi:10.1016/j.jallcom.2016.03.226

[10] Kaiser N. Review of the fundamentals of thin-film growth. Appl. Opt. 2002; 41: 3053–3060. doi:10.1364/AO.41.003053

[11] Rowe DM. Thermoelectrics handbook: macro to nano. In: Rowe DM (Ed) Boca Raton: CRC Press; 2006. 1014 p. doi:10.1201/9781420038903

[12] Thornton JA. Influence of apparatus geometry and deposition conditions on the structure and topography of thick sputtered coatings. J. Vac. Sci. Technol. 1974; 11: 666–670. doi:10.1116/1.1312732

[13] Karabacak T, Singh JP, Zhao Y-P, Wang G-C, Lu T-M. Scaling during shadowing growth of isolated nanocolumns. Phys. Rev. B. 2003; 68: 125408. doi:10.1103/PhysRevB.68.125408

[14] Le PH, Liao C-N, Luo CW, Lin J-Y, Leu J. Thermoelectric properties of bismuth-selenide films with controlled morphology and texture grown using pulsed laser deposition. Appl. Surf. Sci. 2013; 285: 657–663. doi:10.1016/j.apsusc.2013.08.107

[15] Le PH, Liao C-N, Luo CW, Leu J. Thermoelectric properties of nanostructured bismuth–telluride thin films grown using pulsed laser deposition. J. Alloy. Compd. 2014; 615: 546–552. doi:10.1016/j.jallcom.2014.07.018

[16] Tuyen LTC, Le PH, Luo CW, Leu J. Thermoelectric properties of nanocrystalline Bi_3Se_2Te thin films grown using pulsed laser deposition. J. Alloy. Compd. 2016; 673: 107–114. doi:10.1016/j.jallcom.2016.03.006

[17] Ohring M. The materials science of thin films. 2nd ed. San Diego: Academic Press; 2001. 794 p. ISBN: 978-0-12-524975-1

[18] Tritt TM. Thermoelectric phenomena, materials, and applications. Annu. Rev. Mater. Res. 2011; 41: 433–448. doi:10.1146/annurev-matsci-062910-100453

[19] Lind H, Lidin S, Häussermann U. Structure and bonding properties of $(Bi_2Se_3)_m(Bi_2)_n$ stacks by first-principles density functional theory. Phys. Rev. B. 2005; 72: 184101. doi:10.1103/PhysRevB.72.184101

[20] Bos JWG, Zandbergen HW, Lee M-H, Ong NP, Cava RJ. Structures and thermoelectric properties of the infinitely adaptive series $(Bi_2)_m(Bi_2Te_3)_n$. Phys. Rev. B. 2007; 75: 195203. doi:10.1103/PhysRevB.75.195203

[21] Bell LE. Cooling, heating, generating power, and recovering waste heat with thermo-electric systems. Science. 2008; 321: 1457–1461. doi:10.1126/science.1158899

[22] Nolas GS, Sharp J, Goldsmid HJ. Thermoelectrics basic principles and new materials developments. 1st ed. Berlin: Springer; 2001. 293 p. doi:10.1007/978-3-662-04569-5

[23]   Lan Y, Minnich AJ, Chen G, Ren Z. Enhancement of thermoelectric figure-of-merit by a bulk nanostructuring approach. Adv. Funct. Mater. 2010; 20: 357–376. doi:10.1002/adfm.200901512

[24]   Alam H and Ramakrishna S. A review on the enhancement of figure of merit from bulk to nano-thermoelectric materials. Nano Energy. 2013; 2: 190–212. doi:10.1016/j.nanoen.2012.10.005

[25]   Pichanusakorn P, Bandaru P. Nanostructured thermoelectrics. Mater. Sci. Eng. R. 2010; 67: 19–63. doi:10.1016/j.mser.2009.10.001

[26]   Heremans JP, Jovovic V, Toberer ES, Saramat A, Kurosaki K, Charoenphakdee A, Yamanaka S, Snyder GJ. Enhancement of thermoelectric efficiency in PbTe by distortion of the electronic density of states. Science. 2008; 321: 554–557. doi:10.1126/science.1159725

[27]   Nielsch K, Bachmann J, Kimling J, Böttner H. Thermoelectric nanostructures: from physical model systems towards nanograined composites. Adv. Energy Mater. 2011; 1: 713–731. doi:10.1002/aenm.201100207

[28]   He L, Xiu F, Wang Y, Fedorov AV, Huang G, Kou X, Lang M, Beyermann WP, Zou J, Wang KL. Epitaxial growth of Bi_2Se_3 topological insulator thin films on Si (1 1 1). J. Appl. Phys. 2011; 109: 103702. doi:10.1063/1.3585673

[29]   Faleev SV, Léonard F. Theory of enhancement of thermoelectric properties of materials with nanoinclusions. Phys. Rev. B. 2008; 77: 214304. doi:10.1103/PhysRevB.77.214304

[30]   Zebarjadi M, Esfarjani K, Shakouri A, Bian Z, Bahk JH, Zeng G, Bowers J, Lu H, Zide J, Gossard A. Effect of nanoparticles on electron and thermoelectric transport. J. Electron. Mater. 2009; 38: 954–959. doi:10.1007/s11664-008-0656-4

[31]   Sumithra S, Takas NJ, Misra DK, Nolting WM, Poudeu PFP, Stokes KL. Enhancement in thermoelectric figure of merit in nanostructured Bi_2Te_3 with semimetal nanoinclusions. Adv. Energy Mater. 2011; 1: 1141–1147. doi:10.1002/aenm.201100338

[32]   Sun G, Qin X, Li D, Zhang J, Ren B, Zou T, Xin H, Paschen SB, Yan X. Enhanced thermoelectric performance of n-type Bi_2Se_3 doped with Cu. J. Alloys Compd. 2015; 639: 9–14. doi:10.1016/j.jallcom.2015.03.124

[33]   Chang H-C, Chen T-H, Whang W-T, Chen C-H. Superassembling of Bi_2Te_3 hierarchical nanostructures for enhanced thermoelectric performance. J. Mater. Chem. A 2015; 3: 10459–10465. doi:10.1039/c5ta00911a

[34]   Chang H-C, Chen C-H. Self-assembled bismuth telluride films with well-aligned zero- to three-dimensional nanoblocks for thermoelectric applications. CrystEngComm. 2011; 13: 5956. doi:10.1039/c1ce05350g

[35] Deng Y, Liang H-M, Wang Y, Zhang Z-W, Tan M, Cui J-L. Growth and transport properties of oriented bismuth telluride films. J. Alloys Compd. 2011; 509: 5683–4587. doi:10.1016/j.jallcom.2011.02.123

[36] Liu W, Lukas KC, McEnaney K, Lee S, Zhang Q, Opeil CP, Chen G, Ren Z. Studies on the Bi_2Te_3–Bi_2Se_3–Bi_2S_3 system for mid-temperature thermoelectric energy conversion. Energy Environ. Sci. 2013; 6: 552–560. doi:10.1039/c2ee23549h

[37] Wang S, Tan G, Xie W, Zheng G, Li H, Yang J, Tang X. Enhanced thermoelectric properties of $Bi_2(Te_{1-x}Se_x)_3$-based compounds as n-type legs for low-temperature power generation. J. Mater. Chem. 2012; 22: 20943. doi:10.1039/c2jm34608g

[38] Soni A, Yanyuan Z, Ligen Y, Aik MKK, Dresselhaus MS, Xiong Q. Enhanced thermo-electric properties of solution grown $Bi_2Te_{3-x}Se_x$ nanoplatelet composites. Nano Lett. 2012; 12: 1203–1209. doi:10.1021/nl2034859

[39] Li Bassi A, Bailini A, Casari CS, Donati F, Mantegazza A, Passoni M, Russo V, Bottani CE. Thermoelectric properties of Bi–Te films with controlled structure and morphology. J. Appl. Phys. 2009; 105: 124307. doi:10.1063/1.3147870

[40] Tasi C-H, Tseng Y-C, Jian S-R, Liao Y-Y, Lin C-M, Yang P-F, Chen D-L, Chen H-J, Luo C-W, Juang J-Y. Nanomechanical properties of Bi_2Te_3 thin films by nanoindentation. J. Alloys Compd. 2015; 619: 834–838. doi:10.1016/j.jallcom.2014.09.028

[41] Li X, Bhushan B. A review of nanoindentation continuous stiffness measurement technique and its applications. Mater. Charact. 2002; 48: 11–36. doi:10.1016/S1044-5803(02)00192-4

[42] Oliver WC, Pharr GM. An improved technique for determining hardness and elastic modulus using load and displacement sensing indentation experiments. J. Mater. Res. 1992; 7: 1564–1583. doi:10.1557/JMR.1992.1564

[43] Schiøtz J, Vegge T, Di Tolla FD, Jacobsen KW. Atomic-scale simulations of the mechan-ical deformation of nanocrystalline metals. Phys. Rev. B. 1999; 60: 11971–11983. doi:10.1103/PhysRevB.60.11971

[44] Zhang S, Sun D, Fu Y, Du H. Recent advances of superhard nanocomposite coatings: a review. Surf. Coatings Technol. 2003; 167: 113–119. doi:10.1016/S0257-8972(02)00903-9

[45] Masumura RA, Hazzledine PM, Pande CS. Yield stress of fine grained materials. Acta Mater. 1998; 46: 4527–4534. doi:10.1016/S1359-6454(98)00150-5

[46] Greer JR, De Hosson JTM. Plasticity in small-sized metallic systems: intrinsic versus extrinsic size effect. Prog. Mater. Sci. 2011; 56: 654–724. doi:10.1016/j.pmatsci.2011.01.005

[47] Chang SY, Chang T-K. Grain size effect on nanomechanical properties and deformation behavior of copper under nanoindentation test. J. Appl. Phys. 2007; 101: 033507. doi:10.1063/1.2432873

[48] Kumar KS, Suresh S, Chisholm MF, Horton JA, Wang P. Deformation of electrodeposited nanocrystalline nickel. Acta Mater. 2003; 51: 387–405. doi:10.1016/S1359-6454(02)00421-4

[49] Conrad H, Narayan J. On the grain size softening in nanocrystalline materials. Scr. Mater. 2000; 42: 1025–1030. doi:10.1016/S1359-6462(00)00320-1

[50] Hasan MZ, Kane CL. Colloquium: topological insulators. Rev. Mod. Phys. 2010; 82: 3045–3067. doi:10.1103/RevModPhys.82.3045

[51] Hasan MZ, Moore JE. Three-dimensional topological insulators. Annu. Rev. Condens. Matter Phys. 2011; 2: 55–78. doi:10.1146/annurev-conmatphys-062910-140432

[52] Luo CW, Wang HJ, Ku SA, Chen H-J, Yeh TT, Lin J-Y, Wu KH, Juang JY, Young BL, Kobayashi T, Cheng C-M, Chen CH, Tsuei KD, Sankar R, Chou FC, Kokh KA, Tereshchenko OE, Chulkov EV, Andreev YM, Gu GD. Snapshots of Dirac fermions near the Dirac point in topological insulators. Nano Lett. 2013; 13: 5797–802. doi:10.1021/nl4021842

[53] Le PH, Tzeng W-Y, Chen H-J, Luo CW, Lin J-Y, Leu J. Superconductivity in textured Bi clusters/Bi_2Te_3 films. APL Mater. 2014; 2: 096105. doi:10.1063/1.4894779

[54] Tu C-M, Yeh T-T, Tzeng W-Y, Chen Y-R, Chen H-J, Ku S-A, Luo C-W, Lin J-Y, Wu K-H, Juang J-Y, Kobayashi T, Cheng C-M, Tsuei K-D, Berger H, Sankar R, Chou F-C. Manifestation of a second Dirac surface state and bulk bands in THz radiation from topological insulators. Sci. Rep. 2015; 5: 14128. doi:10.1038/srep14128

[55] Chen YL, Analytis JG, Chu J-H, Liu ZK, Mo S-K, Qi XL, Zhang HJ, Lu DH, Dai X, Fang Z, Zhang SC, Fisher IR, Hussain Z, Shen Z-X. Experimental realization of a three-dimensional topological insulator, Bi_2Te_3. Science. 2009; 325: 178–181. doi:10.1126/science.1173034

[56] Hsieh D, Xia Y, Qian D, Wray L, Meier F, Dil JH, Osterwalder J, Patthey L, Fedorov AV, Lin H, Bansil A, Grauer D, Hor YS, Cava RJ, Hasan MZ. Observation of time-reversal-protected single-Dirac-cone topological-insulator states in Bi_2Te_3 and Sb_2Te_3. Phys. Rev. Lett. 2009; 103: 146401. doi:10.1103/PhysRevLett.103.146401

[57] Wang G, Zhu X-G, Sun Y-Y, Li Y-Y, Zhang T, Wen J, Chen X, He K, Wang L-L, Ma X-C, Jia J-F, Zhang SB, Xue Q-K. Topological insulator thin films of Bi_2Te_3 with controlled electronic structure. Adv. Mater. 2011; 23: 2929–2932. doi:10.1002/adma.201100678

[58] Zhang T, Cheng P, Chen X, Jia J-F, Ma X, He K, Wang L, Zhang H, Dai X, Fang Z, Xie X, Xue Q-K. Experimental demonstration of topological surface states protected by time-reversal symmetry. Phys. Rev. Lett. 2009; 103: 266803. doi:10.1103/PhysRevLett.103.266803

[59] Alpichshev Z, Analytis JG, Chu J-H, Fisher IR, Chen YL, Shen ZX, Fang A, Kapitulnik A. STM imaging of electronic waves on the surface of Bi_2Te_3: topologically protected

surface states and hexagonal warping effects. Phys. Rev. Lett. 2010; 104: 016401. doi: 10.1103/PhysRevLett.104.016401

[60] Chiu SP, Lin JJ. Weak antilocalization in topological insulator Bi_2Te_3 microflakes. Phys. Rev. B. 2013; 87: 035122. doi:10.1103/PhysRevB.87.035122

[61] Cha JJ, Kong D, Hong S-S, Analytis JG, Lai K, Cui Y. Weak antilocalization in $Bi_2(Se_xTe_{1-x})_3$ nanoribbons and nanoplates. Nano Lett. 2012; 12: 1107–1111. doi:10.1021/nl300018j

[62] Yu X, He L, Lang M, Jiang W, Xiu F, Liao Z, Wang Y, Kou X, Zhang P, Tang J, Huang G, Zou J, Wang KL. Separation of top and bottom surface conduction in Bi_2Te_3 thin films. Nanotechnology. 2013; 24: 015705. doi:10.1088/0957-4484/24/1/015705

[63] Le PH, Wu KH, Luo CW, Leu J. Growth and characterization of topological insulator Bi_2Se_3 thin films on $SrTiO_3$ using pulsed laser deposition. Thin Solid Films. 2013; 534: 659–665. doi:10.1016/j.tsf.2013.01.104

[64] Lee YF, Punugupati S, Wu F, Jin Z, Narayan J, Schwartz J. Evidence for topological surface states in epitaxial Bi_2Se_3 thin film grown by pulsed laser deposition through magneto-transport measurements. Curr. Opin. Solid State Mater. Sci. 2014; 18: 279–285. doi:10.1016/j.cossms.2014.07.001

[65] Hikami S, Larkin AI, Nagaoka Y. Spin-orbit interaction and magnetoresistance in the two dimensional random system. Prog. Theor. Phys. 1980; 63: 707–710. doi:10.1143/PTP. 63.707

[66] Suzuura H, Ando T. Crossover from symplectic to orthogonal class in a two-dimensional honeycomb lattice. Phys. Rev. Lett. 2002; 89: 266603. doi:10.1103/PhysRevLett. 89.266603

[67] Le PH, Liu P-T, Luo CW, Lin J-Y, Wu KH. Thickness-dependent magnetotransport properties and terahertz response of topological insulator Bi_2Te_3 thin films. J. Alloys Compd. doi:10.1016/j.jallcom.2016.09.109

[68] Lin JJ, Bird JP. Recent experimental studies of electron dephasing in metal and semiconductor mesoscopic structures. J. Phys. Condens. Matter. 2002; 14: R501–596. doi: 10.1088/0953-8984/14/18/201

[69] Steinberg H, Laloë J-B, Fatemi V, Moodera JS, Jarillo-Herrero P. Electrically tunable surface-to-bulk coherent coupling in topological insulator thin films. Phys. Rev. B. 2011; 84: 233101. doi:10.1103/PhysRevB.84.233101

[70] Tang H, Liang D, Qiu RLJ, Gao XPA. Two-dimensional transport-induced linear magnetoresistance in topological insulator Bi_2Se_3 nanoribbons. ACS Nano. 2011; 5: 7510–7516. doi:10.1021/nn2024607

[71] Wang X, Du Y, Dou S, Zhang C. Room temperature giant and linear magnetoresistance in topological insulator Bi_2Te_3 nanosheets. Phys. Rev. Lett. 2012; 108: 266806. doi: 10.1103/PhysRevLett.108.266806

[72] Assaf BA, Cardinal T, Wei P, Katmis F, Moodera JS, Heiman D. Linear magnetoresistance in topological insulator thin films: quantum phase coherence effects at high temperatures. Appl. Phys. Lett. 2013; 102: 012102. doi:10.1063/1.4773207

[73] Abrikosov AA. Quantum magnetoresistance. Phys. Rev. B. 1998; 58: 2788–2794. doi: 10.1103/PhysRevB.58.2788

[74] Abrikosov AA. Quantum linear magnetoresistance; solution of an old mystery. J. Phys. A Math. Gen. 2003; 36: 9119–9131. doi:10.1088/0305-4470/36/35/301

[75] Wang CM, Lei XL. Linear magnetoresistance on the topological surface. Phys. Rev. B. 2012; 86: 035442. doi:10.1103/PhysRevB.86.035442

[76] Qi X-L, Hughes TL, Raghu S, Zhang S-C. Time-reversal-invariant topological superconductors and superfluids in two and three dimensions. Phys. Rev. Lett. 2009; 102: 187001. doi:10.1103/PhysRevLett.102.187001

[77] Wilczek F. Majorana returns. Nat. Phys. 2009; 5: 614–618. doi:10.1038/nphys1380

[78] Koren G, Kirzhner T, Lahoud E, Chashka KB, Kanigel A. Proximity-induced superconductivity in topological Bi_2Te_2Se and Bi_2Se_3 films: robust zero-energy bound state possibly due to Majorana fermions. Phys. Rev. B. 2011; 84: 224521. doi:10.1103/PhysRevB.84.224521

[79] Noro H, Sato K, Kagechika H. The thermoelectric properties and crystallography of Bi-Sb-Te-Se thin films grown by ion beam sputtering. J. Appl. Phys. 1993; 73: 1252–1260. doi:10.1063/1.353266